Acta Pharmaceutica Sinica B 2026;16(2):1022−1045

Chinese Pharmaceutical Association
Institute of Materia Medica, Chinese Academy of Medical Sciences

Acta Pharmaceutica Sinica B

www.elsevier.com/locate/apsb
www.sciencedirect.com

ORIGINAL ARTICLE

Multifunctional extracellular vesicles inhibiting autophagy ameliorate immunotherapy in non-small cell lung cancer

Simiao Wang[a], Jiayi Chen[a], Yaxin Cui[a], Jianming Xing[a], Jiayi Liu[a], Hao Jiang[a], Hongqun Yang[b], Huan Zhang[a], Man Sun[a], Jialin Li[c], Wei Liu[c], Zhou Chen[d], Wei Sun[e,*], Xiaobing Wang[f,*], Zhaogang Yang[a,*]

[a]*School of Life Sciences, Jilin University, Changchun 130012, China*
[b]*Department of Endoscopy Center, China-Japan Union Hospital of Jilin University, Changchun 130033, China*
[c]*Department of Thoracic Surgery, The First Hospital of Jilin University, Changchun 130021, China*
[d]*School of Mechanical and Power Engineering, Nanjing Tech University, Nanjing 211800, China*
[e]*Department of Molecular Biology, College of Basic Medical Sciences, Jilin University, Changchun 130021, China*
[f]*State Key Laboratory of Molecular Oncology, National Cancer Center/National Clinical Research Center for Cancer/Cancer Hospital, Chinese Academy of Medical Sciences and Peking Union Medical College, Beijing 100021, China*

Received 3 June 2025; received in revised form 2 August 2025; accepted 11 September 2025

KEY WORDS

Autophagy;
Cancer immunotherapy;
Engineered extracellular vesicles;
Drug delivery;
Non-small cell lung cancer;
Interleukin-7;
Tumor microenvironment;
PD-L1

Abstract The modulation of tumor autophagy to enhance antitumor immunity has garnered significant attention, underscoring its critical role in cancer immunotherapy. However, advanced strategies for precise autophagy-regulating drug delivery remain a pressing need. Here, we introduce a targeted small extracellular vesicles (sEVs)-based drug delivery system capable of simultaneously loading antibodies and nucleic acid drugs while ensuring their accurate release in the tumor microenvironment (TME). We developed a dual-stimulation electroporation system that integrates nanosecond electric pulses and ultrasound to enhance sEV production, yielding *IL-7* mRNA-enriched sEVs that overexpress CD64 receptors for efficient capture of anti-PD-L1 antibodies. These multifunctional autophagy-inhibiting and immunomodulatory sEVs (AI-sEVs) are designed to inhibit autophagy and modulate immune responses in non-small cell lung cancer. Upon delivery to the TME, AI-sEVs mediate the enzymatic cleavage of peptide bonds, releasing *IL-7* mRNA. This process induces autophagy suppression and restores MHC-I expression, which synergizes with anti-PD-L1 immune checkpoint inhibition to enhance

*Corresponding authors.
E-mail addresses: s_wei@jlu.edu.cn (Wei Sun), wangxb@cicams.ac.cn (Xiaobing Wang), zhaogangyang@jlu.edu.cn (Zhaogang Yang).

Peer review under the responsibility of Chinese Pharmaceutical Association and Institute of Materia Medica, Chinese Academy of Medical Sciences.

https://doi.org/10.1016/j.apsb.2025.12.013

antitumor efficacy. In conclusion, this study proposes an innovative methodology that utilizes engineered sEVs for the co-delivery of protein antibodies and genetic materials. This approach establishes a promising strategy for advancing cancer immunotherapy by targeting the modulation of autophagy.

1. Introduction

Non-small cell lung cancer (NSCLC), accounting for approximately 85% of diagnosed lung cancer cases, remains one of the leading causes of cancer-related mortality worldwide, with a dismal 5-year survival rate of only 16%[1-3]. Conventional treatments, such as platinum-based chemotherapy, have demonstrated limited efficacy and are often accompanied by severe adverse effects[4,5]. The emergence of immune checkpoint inhibitors (ICIs) has revolutionized the therapeutic landscape of NSCLC by restoring antitumor immunity. Inhibitors targeting programmed cell death-1 (PD-1), like nivolumab and pembrolizumab[6,7], or its ligand PD-L1, such as durvalumab and atezolizumab[8,9], have been approved as first- or second-line therapies for advanced NSCLC. Despite these advances, clinical outcomes remain suboptimal, with only approximately 20% of patients achieving durable benefits, and many experience relapse due to acquired resistance[10]. The tumor microenvironment (TME) plays a crucial role in shaping immunotherapy outcomes, often fostering immune evasion through various mechanisms. These include high infiltration of immunosuppressive cells like tumor-associated macrophages (TAMs)[11], decreased expression of anti-tumor cytokines and tumor-associated antigens[12], impaired T cell function[13], as well as metabolic reprogramming[14], hypoxia, and an acidic extracellular milieu-all of which contribute to an immunosuppressive TME (ITME) that poses a significant challenge to immunotherapy[15,16]. Accordingly, reversing these conditions could significantly enhance the effectiveness of immunotherapy.

Autophagy, a fundamental cellular recycling mechanism, plays an essential role in cancer progression and tumor immunity[17]. During early tumorigenesis, autophagy acts as a tumor suppressor by eliminating damaged organelles and maintaining genomic integrity. However, in established tumors—including NSCLC—autophagy shifts to promote tumor survival during metabolic stress, treatment-induced damage, and immunosurveillance resistance. Notably, autophagy modulates the TME by altering immune cell function and cytokine secretion, while itself being reciprocally regulated by immune components[18]. In NSCLC, selective autophagy promotes immune evasion by recruiting major histocompatibility complex (MHC) class I antigen complexes for lysosomal degradation *via* the ubiquitin-binding receptor NBR1, thereby preventing their recognition by effector T cells[19,20]. Furthermore, secretory autophagy fosters an immunosuppressive microenvironment by promoting neutrophil-mediated immunosuppression, driving M2 macrophage polarization, and inhibiting $CD8^+$ T cells proliferation[21,22]. Consequently, precise modulation of autophagy—preserving autophagic homeostasis in normal cells while selectively inhibiting tumor-promoting autophagy—has emerged as a promising approach to reprogram the TME and improve the efficacy of immunotherapy in NSCLC.

Emerging evidence indicates that interleukin-7 (IL-7), an immunomodulatory cytokine, can regulate tumor autophagy, aligning to reprogram the TME[23]. As a homeostatic cytokine essential for T cell survival, IL-7 holds strong therapeutic potential in cancer immunotherapy. It selectively promotes the expansion of naïve and memory $CD8^+$ T cells. It enhances the expression of MHC-I on tumor cells by counteracting autophagy-mediated degradation, thereby synergizing with immune checkpoint blockade (ICB) therapies[24]. While IL-2 is commonly used to stimulate T cell proliferation[25], its clinical utility is severely limited by dose-dependent toxicities, including vascular leak syndrome (VLS)[26]. When combined with PD-1 inhibitors, IL-2 may further exacerbate VLS due to heightened immune activation[27]. Moreover, IL-2 preferentially expands immunosuppressive regulatory T cells (Tregs), which can undermine antitumor responses[28]. In contrast, IL-7 avoids these limitations. It does not induce vascular toxicities, supports sustained administration, and does not promote Treg expansion. These properties position IL-7 as a compelling candidate for reversing T cell exhaustion and restoring antigen presentation in NSCLC.

While targeting autophagy offers a significant opportunity for reversing the ITME, the development of a robust drug delivery system remains crucial for its effective implementation. Macromolecular therapeutics, such as antibodies and nucleic acids, faced challenges including short half-lives, instability, and immunogenicity, which limit their effectiveness in cancer immunotherapy[29,30]. Small extracellular vesicles (sEVs), naturally derived nanovesicles with bilayer membranes released by virtually all cells[31], have emerged as promising drug delivery carriers owing to their stability in circulation, high biocompatibility, minimal toxicity, low immunogenicity, and ability to cross biological barriers[32]. Moreover, sEVs exhibit efficient cellular uptake and homing capacity, fusing with recipient cell membranes to protect payloads from lysosomal degradation, thereby overcoming key obstacles in immunotherapeutic drug delivery[33]. However, challenges persist, including the limited scalability of sEV production and the lack of successful platforms for co-delivering mRNA and antibody drugs.

In this study, we introduced a novel dual-stimulation electroporation system (DES) that integrated nanosecond pulses with ultrasound to enhance sEV yield and enable precise cargo loading, thereby optimizing sEV-based cancer therapy. Leveraging this advanced stimulation technique, we engineered multifunctional autophagy-inhibiting and immunomodulatory sEVs (AI-sEVs) with high CD64 surface expression, facilitating the targeted delivery of anti-PD-L1 antibodies and *IL*-7 mRNA. Upon reaching the NSCLC TME, AI-sEVs exerted dual therapeutic effects: surface-conjugated anti-PD-L1 antibodies block immune checkpoints, while encapsulated *IL*-7 mRNA undergoes cathepsin B-mediated enzymatic cleavage of peptide linkages within tumor cell cytoplasm, enabling its release and subsequent translation. The expressed IL-7 protein inhibited tumor autophagy, restored MHC-I expression on NSCLC cells, enhanced effector T cell recruitment, and reprogrammed the ITME to improve immunotherapeutic outcomes (Fig. 1). Our results demonstrate significant

immunotherapeutic efficacy in both orthotopic and patient-derived xenografts (PDX) models of NSCLC. In summary, our findings highlight a successful strategy for the co-delivery of macromolecular nucleic acids and proteins, providing a novel approach to advancing autophagy-based immunotherapy and improving clinical outcomes in NSCLC.

2. Materials and methods

2.1. Cell culture and plasmid construction

Human embryonic kidney cell (HEK293T), mouse embryonic fibroblast (MEF), and human lung cancer cells (A549) were obtained from American Type Culture Collection (ATCC) (Manassas, VA, USA). Lewis lung carcinoma (LLC) and its luciferase-expressing cell line (LLC-luc) were obtained from Shanghai Jinyuan Biotechnology Co., Ltd. (Shanghai, China). HEK293T, MEF, A549, LLC and LLC-luc cells were cultured in Dulbecco's modified Eagle's medium (DMEM) (Invitrogen, 11965092, Carlsbad, CA, USA) supplemented with 10% fetal bovine serum (FBS) (Invitrogen, A5670701, Carlsbad, CA, USA) and 1% penicillin−streptomycin (Invitrogen, R01510, Carlsbad, CA, USA) under sterile conditions at 37 °C with 5% CO_2. To establish a stable cell population expressing the luciferase reporter gene, puromycin (MCE, HY-B1743, NJ, USA) selection (at concentrations of 2−4 μg/mL) was performed every 10 passages.

Plasmids including pLV3-CMV-YSA-CD64(human/mouse)-$(GFLG)_3$-Rev ARM-Puro, pCMV-IL-7(human/mouse)-RRE-IIB-Neo, and pCDH-CMV-mRFP1-EGFP-LC3B-Puro were obtained from Shenzhen DINGKE Biotechnology Co., Ltd. (Shenzhen, China) (Supporting Information Fig. S1). In these constructs, the sequence encoding the Rev ARM peptide (DTRQA RRNRR RRWRE RQRAA AAR) was introduced at the C-terminus of CD64. Similarly, the RRE-IIB (5′-GGUCU GGGCG CAGCG UCAAU GACGC UGACG GUACA GGCC-3′) was inserted at the 3′ end of IL-7. To target NSCLC cells, YSA peptide (YSAYPDSVPMMS), which targets the EphA2 receptor overexpressed in NSCLC, was modified at the CD64 N-terminus[34]. Additionally, a polypeptide $(GFLG)_3$ (GFLGGFLGGFLG) that can be hydrolyzed explicitly by cathepsin B was inserted between CD64 and Rev ARM peptide to facilitate gene drug release in the TME.

2.2. Human participants

Patients for RNA sequencing (RNA-seq) and immunohistochemistry (IHC) experiments to investigate responses to anti-PD-L1 immunotherapy were recruited from the National Cancer Center/

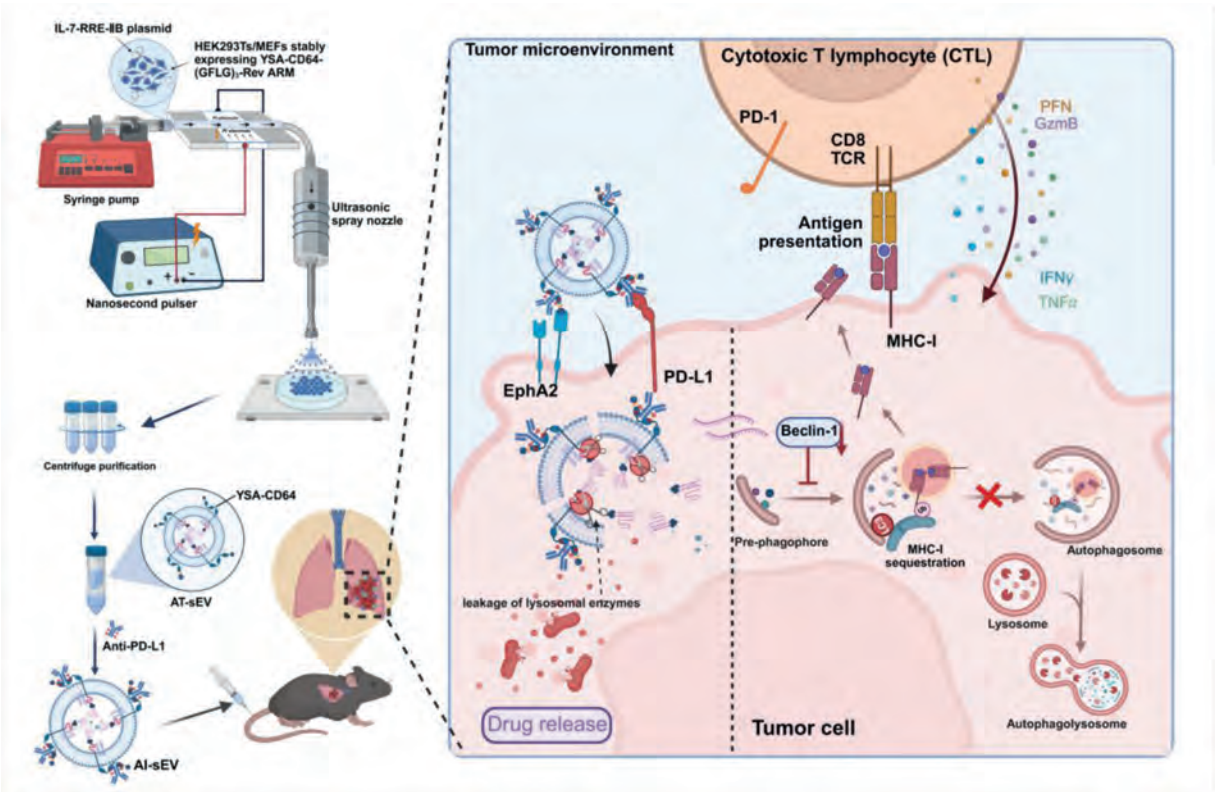

Figure 1 Schematic representation of the production and therapeutic mechanism of AI-sEVs in NSCLC. AI-sEVs, multifunctional sEVs engineered to inhibit autophagy and enhance antitumor immune responses, are produced using a DES integrating nanosecond electric pulses and ultrasound. This process stimulates robust sEV secretion and facilitates *IL*-7 mRNA loading through specific Rev ARM peptide−RRE-IIB RNA complexation. Concurrently, strategic overexpression of CD64 protein on sEV membranes enables selective surface conjugation of anti-PD-L1 antibodies. Upon reaching the NSCLC TME, AI-sEVs undergo enzymatic cleavage by cathepsin B *via* a GFLG peptide linker, triggering the release of *IL*-7 mRNA. The targeted release induces autophagy suppression and restores MHC-I expression on tumor cells. This mechanism synergizes with anti-PD-L1 immune checkpoint inhibition, thereby reactivating cytotoxic immune responses. HEK293T, Human embryonic kidney cell; MEF, mouse embryonic fibroblast; RRE-IIB, Rev Response Element-Stem-Loop IIB; Rev ARM, Rev Arginine-Rich Motif; EpHA2, Ephrin type-A receptor 2; CTL, Cytotoxic T Lymphocyte.

National Clinical Research Center for Cancer/Cancer Hospital, Beijing, China. Patients receiving neoadjuvant immunotherapy with a pathological remission rate exceeding 90% were classified into the better-responsive group. In comparison, those with a remission rate below 10% were assigned to the less-responsive group. Moreover, differential expression of IL-7 in RNA-seq data from paired responders and non-responders was defined using stringent criteria: an adjusted *P*-value (*P*-adj) < 0.05 and an absolute fold change ($|FC| \geq 2$. When patients were stratified based on their response to anti-PD-L1 immunotherapy, IL-7 met these criteria with a $\log_2$ fold change ($\log_2FC$) of 3.135 (*P*-adj $= 0.0015$) between responders and non-responders. Following approval from the institutional ethics board (Approval No. 22/456-3658), biopsy and surgical resection specimens were obtained from participants who provided written informed consent. Patient recruitment was conducted inclusively, irrespective of sex, ancestry, socioeconomic status, age, or ethnicity.

Additionally, samples used for differential analysis of tumor and precancerous lesions, as well as for the PDX tumor model, were obtained from the First Hospital of Jilin University, Changchun, Jilin, China. Following approval from the institutional ethics board (Approval No. 24K227-001), biopsy and surgical resection specimens were obtained from participants who provided written informed consent. Patient recruitment was conducted inclusively, irrespective of sex, ancestry, socioeconomic status, age, or ethnicity. NSCLC tissue samples were collected upon surgery.

2.3. Fabrication of DES

A section of a nanosecond pulse in a dual-stimulation system device was fabricated using a polymethyl methacrylate (PMMA) block, shaped through Computer Numeric Control (CNC) machining. A platinum wire (50 μm diameter) was embedded into the PMMA block *via* hot embossing. A micro-milling machine was employed to create a microchannel (200 μm width × 200 μm depth × 5 cm length) perpendicular to the embedded platinum wire. The channel was subsequently cut at this intersection to form two electrodes, which were connected to a nanosecond pulse generator to facilitate electroporation. An ultrasonic spray nozzle was attached to the fabricated PMMA block further to stimulate sEV secretion after exposure to the nanosecond pulses. A syringe pump (KD Scientific, KDS 100 Legacy, Holliston, MA, USA) precisely controlled the flow rate of the cellular solution. At the same time, a Petri dish beneath the ultrasonic nozzle allowed direct inoculation of the atomized cell suspension. IL-7-RRE-IIB plasmids were mixed with HEK293Ts/MEFs cells stably expressing YSA-CD64-$(GFLG)_3$-Rev ARM protein. The mixture was processed through the device under optimized conditions, and the cells were cultured to enable plasmid expression and sEV production. The supernatant containing secreted sEVs was subsequently collected for further analysis or therapeutic applications.

2.4. Transfection of cells via the DES system

Cell suspensions were prepared in basic medium at 1×10^7 cells/mL. Subsequently, plasmid DNA (100 μg/mL) was introduced into this suspension. The combined solution was infused into the ultrasonic nozzle *via* a single-channel syringe pump operating at 2 mL/h. Before reaching the ultrasound nozzle, nanosecond pulsed electroporation was applied to enhance plasmid uptake by the cells. Following electroporation, the treated cells were allowed to settle freely in culture dishes and incubated in fresh complete medium for 24 h. Subsequently, the conditioned medium was collected for sEV isolation.

2.5. sEV isolation and purification

Cell supernatants were collected 24 h post-transfection, and sEVs were purified *via* ultracentrifugation. Cell culture supernatants underwent initial centrifugation ($300\times g$, 10 min) (Eppendorf, 5810R, Hamburg, Germany) to pellet intact cells. The clarified supernatant was subjected to a $3000\times g$ (Eppendorf) spin for 10 min, removing smaller debris and apoptotic vesicles. Subsequent centrifugation at $10{,}000\times g$ (30 min) (Eppendorf) cleared larger microvesicles. Following 0.22 μm membrane filtration of large extracellular vesicles, the filtrate was ultracentrifuged at $100{,}000\times g$ for 70 min in a Beckman ultracentrifuge (Beckman Coulter, OptimaTM MAX-XP, Brea, CA, USA) to pellet the sEVs. After discarding the supernatant, the resulting pellet was resuspended in buffer to obtain purified sEVs.

To prepare AI-sEV, the isolated sEVs were co-incubated with anti-PD-L1 antibodies for 2 h at 37 °C. Following incubation, an additional ultracentrifugation (Beckman Coulter) step was performed for 2 h to remove any unbound antibody, ensuring the purity of the final AI-sEV preparation. In the transition from blank sEVs to AI-sEVs, various types of sEVs are involved. To aid clarity, a reference table (Table 1) has been compiled, listing their abbreviations, full names, and associated modifications.

2.6. Morphological characterization and particle size analysis of sEVs

Before sEV characterization, sterile-filtered PBS was used to adjust sample particle concentrations within the analytical range for nanoparticle tracking analysis (NTA), typically ranging

Table 1 Abbreviations for sEVs with different modifications.

Abbreviation	Full name	Key modification
sEV	Blank sEVs	None (native HEK293T sEVs)
CD64-sEV	CD64-overexpressing sEVs	CD64 anchored on the sEV membrane
T-sEV	Lung tumor-targeted sEVs	YSA-CD64-$(GFLG)_3$-Rev ARM tandem protein anchored to the sEV membrane
IL-7-sEV	IL-7-overexpressing sEVs	*IL-7-RRE-IIB* mRNA loaded into T-sEVs
AT-sEV	Autophagy-targeted sEVs	*IL-7-RRE-IIB* mRNA loaded into T-sEV and specifically coupled to CD64 through RRE-IIB/Rev ARM interaction
AI-sEV	Multifunctional autophagy-inhibiting and immunomodulatory sEVs	Anti-PD-L1 antibody conjugated to AT-sEVs *via* CD64 anchoring

between 1×10^7 and 1×10^9 particles/mL. Diluted aliquots were analyzed in a NanoSight NS300 chamber (Malvern Panalytical, NS300, Malvern, UK) configured with 488 nm laser excitation and sCMOS camera acquisition. Before sample loading, the instrument was calibrated using standard polystyrene beads of known size (100 nm diameter). Data collection and quantification utilized NTA v3.4 (Malvern Panalytical).

For cryo-transmission electron microscopy (cryo-TEM) analysis, sEV specimens (3 μL, 1×10^{10} particles/mL) were deposited on Quantifoil R2/2 Au 300-mesh grids. Vitrobot Mark IV (Thermo Fisher, Vitrobot Mark IV, Waltham, MA, USA)-assisted blotting (4 s, 100% humidity, 4 °C) preceded rapid vitrification in liquid ethane (−180 °C), with cryopreservation in liquid nitrogen until transmission electron microscopy (TEM) analysis. The grids were subsequently transferred to a Talos L120C G2 cryo-TEM (Thermo Fisher, Talos L120C G2, Waltham, MA, USA) equipped with a Ceta-D CMOS camera and operated at an acceleration voltage of 120 kV. To minimize beam-induced damage, the low-dose mode was employed. Tilt series (−60° to +60°, 2° increments) were acquired at 73,000× magnification (pixel size: 0.34 nm) using SerialEM v4.0 software, targeting ice-embedded sEVs with optimal thickness (50−150 nm).

2.7. RNA expression levels by RT-qPCR

Quantitative assessment of *IL-7* and *classical HLA-I loci (HLA-A, -B, -C)* transcript levels in sEV and cellular fractions was performed *via* SYBR Green-based Quantitative Real-time polymerase chain reaction (RT-qPCR). Total RNA extraction employed the EasyPure miRNA Kit (TransGen Biotech, ER601, Beijing, China), with subsequent first-strand cDNA synthesis using TransScript® SuperMix (TransGen Biotech, AT341, Beijing, China). Amplification reactions on a CFX96 thermocycler (Thermo Fisher, CFX96, Waltham, MA, USA) utilized PerfectStart® Green qPCR SuperMix (TransGen Biotech, AQ601, Beijing, China) under optimized cycling: 95 °C (30 s) initiation; 40 cycles of 95 °C (5 s) denaturation and 60 °C (30 s) annealing/extension. Reaction specificity was confirmed by melt curve analysis.

The loading capacity of *IL*-7 mRNA in sEVs was quantified by RT-qPCR and expressed as the number of *IL*-7 mRNA copies per 100 sEVs. A standard curve was generated using synthetic *IL*-7 mRNA of known copy number. Total RNA was extracted from sEVs according to the manufacturer's instructions and reverse-transcribed into cDNA. QPCR was then performed using primers and probes specific for *IL*-7 mRNA alongside an internal reference. The absolute copy number was calculated based on the standard curve derived from serially diluted *in vitro*-transcribed *IL*-7 mRNA. The results are presented as the mean number of *IL*-7 mRNA copies per 100 sEVs.

The mRNA levels of sEVs were normalized to *U6* small nuclear RNA, while cellular expression values were referenced to *GAPDH*. Oligonucleotide sequences (synthesized and HPLC-purified by Sangon Biotech, Shanghai, China) were as follows (Table 2).

2.8. Protein expression levels by Western blot

Total protein lysates from cellular and sEV fractions were solubilized in RIPA lysis buffer (Thermo Fisher, 89900, Waltham, MA, USA) containing 1 × protease inhibitor cocktail (NCM Biotech, P001, Suzhou, China). Protein quantification was performed using a bicinchoninic acid (BCA) protein assay system (Thermo Fisher, 23235, Waltham, MA, USA), with 20 μg of cells or 40 μg of sEVs loaded per lane. SDS-PAGE was performed at 120 V for 90 min, followed by protein transfer onto 0.45 μm PVDF membranes at 100 V for 100 min. Membranes were blocked for 1 h and then incubated *via* 16 h cold incubation (4 °C) with primary antibodies: anti-CD9 (Abcam, ab307085, Cambridge, UK), anti-CD63 (Abcam, ab315108, Cambridge, UK), anti-CD81 (Abcam, ab109201, Cambridge, UK), anti-Calnexin (Proteintech, 10427-2-AP, Wuhan, China), anti-TSG101 (Abcam, ab125011, Cambridge, UK), anti-LC3B (Proteintech, 14600-1-AP, Wuhan, China), anti-ATG7 (Abclonal, ab125011, Wuhan, China), anti-Beclin-1 (Abclonal, A21191, Wuhan, China), anti-p62/SQSTM1 (Abclonal, A21702, Wuhan, China), anti-IL-7 (Abclonal, A22570, Wuhan, China), anti-HLA-ABC (Proteintech, 15240-1-AP, Wuhan, China), anti-CD64 (Abclonal, A1197, Wuhan, China), anti-GAPDH (Proteintech, 60004-1-Ig, Wuhan, China). After initial antibody binding, membranes underwent sequential washing and probing with HRP-conjugated secondaries (Cell Signaling Technology, 7076, Danvers, MA, USA). Protein band visualization employed ECL Prime chemiluminescent substrate under a Tanon2500 imaging system (Shanghai, China).

2.9. Detection of mRNA in sEVs

Cationic lipoplex nanoparticles containing molecular beacons (MB) for *IL*-7 mRNA detection were prepared by injecting MBs/lipids mixture to PBS as previously described[35,36]. Briefly, 9.75 μL of *Cy5-IL-7* mRNA MB stock solution (100 μmol/L, in PBS) was first mixed with 29.5 μL lipid ethanol stock solution (DOTMA: Cholesterol: Biotin-PEG6-SH = 49:49:2, molar ratio). The MB/lipids mixture was then injected into 675 μL PBS and vortexed for 10 s. The solution was further sonicated for 5 min at room temperature, and mixed with EV solution at a ratio of 1:1 (*v*/*v*). After rotating at room temperature for 2 h, the samples were pelleted by ultracentrifugation, washed with cold PBS, resuspended in PBS, and visualized using confocal laser scanning microscopy (CLSM) (FV3000, Olympus, Tokyo, Japan). The MB that detects *IL*-7 mRNA was as follows: 5′-Cy5-CGCGATC-GACAGCATGAAAGAAATTGGTAGC-GATCGCG-BHQ3-3′.

Table 2 Primer sequences adopted in RT-qPCR.

Name	Forward primer	Reverse primer
U6	CTCGCTTCGGCAGCACAT	TTTGCGTGTCATCCTTGCG
GAPDH	GTCTCCTCTGACTTCAACAGCG	ACCACCCTGTTGCTGTAGCCAA
IL-7	GACAGCATGAAAGAAATTGGTAGC	CAACTTGCGAGCAGCACGGAAT
HLA-A	AGATACACCTGCCATGTGCAGC	GATCACAGCTCCAAGGAGAACC
HLA-B	CTGCTGTGATGTGTAGGAGGAAG	GCTGTGAGAGACACATCAGAGC
HLA-C	GGAGACACAGAAGTACAAGCGC	ACATCCTCTGGAGGGTGTGAGA

2.10. Cellular uptake analysis

The cellular uptake of AI-sEVs by lung cancer cells was evaluated using PKH67-labeled AI-sEV complexes. AI-sEVs were tagged with PKH67 green fluorescent dye (Sigma−Aldrich, MINI67, St. Louis, MO, USA) by mixing 100 μg of AI-sEVs with 2 μmol/L PKH67 dye in 1 mL Diluent C and incubating at 25 °C (20 min). Unbound dye was removed *via* ultracentrifugation (100,000×*g*, 4 °C, 70 min; Beckman Coulter, Optima XE-100, Brea, CA, USA), and the labeled AI-sEVs (PKH67-AI-sEVs) was resuspended in sterile PBS.

PKH67-AI-sEV (20 μg/mL) was applied to A549/LLC cells (6-well plates, 10^5 cells/well) for 1−4 h (37 °C/5% CO_2). Cells were then PBS-washed , fixed with 4% paraformaldehyde, and quantitatively analyzed *via* CytoFLEX S Flow Cytometry (Beckman Coulter, CytoFLEX S, Brea, CA, USA). Additionally, cellular uptake of PKH67-AI-sEV was visualized using CLSM (Olympus, FV3000, Tokyo, Japan).

To investigate the cellular uptake pathway of AI-sEVs in A549 and LLC cells, cells were pre-incubated with transferrin-Alexa Fluor 555 (0.1 mg/mL), cholera toxin subunit B-Alexa Fluor 555 conjugates (CT-B) (0.005 mg/mL), or dextran-Alexa Fluor 555 (1 mg/mL) (all from Invitrogen, Carlsbad, CA, USA) for 1 h to label specific uptake pathways. After washing to remove unbound compounds, cells were incubated with PKH67-AI-sEV for 4 h. Nuclear staining was performed using Hoechst 33342, and images were captured using CLSM.

2.11. Autophagy flux assay

A549/LLC cultures were expanded in 12-well plates to 70%−80% monolayer confluence under standard incubation conditions. The cells were then transfected with a plasmid encoding CMV-mRFP1-EGFP-LC3B (Shenzhen DINGKE Biotechnology Co., Ltd.). Cells underwent protocol-defined incubation following transfection to achieve fluorescence-competent LC3B-chimeric protein expression. To induce autophagy, cells were treated with 500 nmol/L rapamycin for 24 h. Post-treatment cellular fixation employed 4% paraformaldehyde solution, with subsequent nuclear chromatin counterstaining using Hoechst 33342 fluorophore. Fluorescent signals were observed using CLSM. Relative quantification was performed by counting the number of red and yellow puncta per cell, corresponding to autolysosomes and autophagosomes, respectively.

2.12. TEM assay

Cells or lung cancer tissues were fixed overnight in 2% glutaraldehyde following the removal of the culture medium. Following pre-embedding in agar and fixation with 1% osmium tetroxide, the samples were embedded in resin blocks and sectioned into ultrathin slices. The slices were transferred to 150-mesh copper support grids and stained with a saturated alcoholic solution of 2% uranium acetate for 8 min in the dark, followed by washing and staining with a 2.6% lead citrate solution (8 min) under carbon dioxide-free conditions. Post-wash protocols culminated in 16 h atmospheric drying under dust-free conditions. Observations were conducted using TEM (HITACHI, HT7800, Tokyo, Japan), and images were acquired for further analysis.

2.13. In vitro anti-tumor effect study

Male H11-OT1 mice (3−4 weeks) were commercially sourced (GemPharmatech Co., Ltd., Nanjing, China) and acclimatized for 7 days in specific pathogen-free (SPF) facilities. All animal experimental procedures received prior approval from Jilin University's Institutional Animal Care and Use Committee (IACUC) (Approval No. SY202410004).

To isolate $CD8^+$ T cells from OT-1 mice, spleens were aseptically harvested and washed twice with sterile PBS. Splenic tissue was mechanically dissociated through a 70 μm nylon cell strainer. Post-harvest splenocytes were sedimented (300×*g*, 5 min), red blood cell (RBC)-lysed (sterile buffer, 10 min), washed twice with ice-cold PBS, mechanically filtered, and counted to achieve a concentration of approximately 1×10^8 cells per spleen. Naïve $CD8^+$ T cells were isolated following the manufacturer's protocol (Miltenyi Biotec, Cat. No. 130-096-543, Bergisch Gladbach, Germany).

LLC cells were treated with either AI-sEVs or anti-PD-L1 antibodies for 24 h. T cell receptor (TCR) engagement of OT-1 $CD8^+$ T cells was achieved through 24 h co-incubation with the cognate MHC-I-presented $OVA_{257-264}$ peptide. LLC cells and OT-1-derived $CD8^+$ T cells underwent paracrine co-culture (24 h, Transwell) with T cells positioned apically. TCR engagement was triggered *via* apical administration of CD3/CD28 co-stimulatory ligands (1 μg/mL). After 60 h, supernatants were collected to measure levels of IL-7, IL-2, IFN-γ, and TNF-α cytokines using an enzyme-linked immunosorbent assay (ELISA) kit. Tumor cell viability was assessed using the MTS assay.

2.14. In situ lung cancer model

Male C57BL/6 mice (3−4 weeks) were commercially sourced (Liaoning Changsheng Biotechnology Co., Ltd., Benxi, China) and acclimatized for 7 days in SPF facilities. All animal experimental procedures received prior approval from Jilin University's IACUC (Approval No. SY202312015).

Orthotopic lung tumors were established in anesthetized C57BL/6 mice (4% isoflurane induction and 1.5%−2% maintenance). Following left thoracotomy *via* a 5-mm incision at the 4th intercostal space, 50 μL PBS containing LLC-luc cells (1×10^6) was infused into the pulmonary parenchyma using insulin syringes. The needle was retained for 10 s post-injection to minimize reflux. The thoracic cavity was closed in layers, and negative pressure was restored before skin suture. To reduce pain and distress, all mice received postoperative analgesia. Buprenorphine hydrochloride was administered subcutaneously at a dose of 0.05 mg/kg body weight. The initial dose was given immediately after skin closure while the animals remained under anesthesia. Additional doses were administered every 12 h for 48 h postoperatively. Postoperative monitoring included respiratory rate assessment, activity evaluation, and exclusion of mice exhibiting pneumothorax or infection.

Tumor engraftment was confirmed by an *in vivo* imaging system (Revvity, IVIS Spectrum, Waltham, MA, USA) at Day 3 post-inoculation. Successfully modeled mice were randomized into five treatment groups ($n = 6$ per group): PBS (control), sEV-treated, AT-sEV-treated, AI-sEV-treated (2.5 mg/kg), and anti-PD-L1 antibody-treated (10 mg/kg). The AI-sEV co-loaded with *IL*-7 mRNA and anti-PD-L1 antibody contained approximately 8.95×10^{11} copies of *IL*-7 mRNA and 4.33 μg of anti-PD-L1 antibody per injection. The treatment was administered *via* tail vein injection every three days, with a total injection volume of 100 μL per dose. Longitudinal tumor progression was quantified by bioluminescence signal intensity (1×10^6 p/s) measured at Days 3, 7, 11, 15, 19, and 23. Body weight and food intake were

monitored throughout the study. Kaplan−Meier methodology quantified survival outcomes. Following the 23-day intervention period, terminally anesthetized mice were euthanized. Major organs (brain, heart, liver, spleen, lungs, and kidneys) and tumor specimens were harvested for comprehensive histopathological analysis.

2.15. *In vivo biodistribution analysis*

D-luciferin (150 mg/kg) was delivered *via* intraperitoneal administration to enable bioluminescent imaging, and bioluminescence was detected by the IVIS imaging system (Revvity, IVIS Spectrum, Waltham, MA, USA) to confirm the successful establishment of the orthotopic lung cancer model. Subsequently, PKH26-labeled blank sEVs (sEVs) and AI-sEVs (2.5 mg/kg) were injected *via* the tail vein. Fluorescence distribution of PKH26 was monitored at 1 and 4 h post-injection using the IVIS imaging system. 4 h after injection, mice were euthanized, and major organs (brain, heart, liver, spleen, lungs, and kidneys) and tumor were harvested to assess fluorescence distribution using the same imaging system[37].

2.16. *PDX lung cancer model*

Male NOD-Prkdcem1Il2rgem1 (NYG) mice (3−4 weeks) were commercially sourced (Liaoning Changsheng Biotechnology Co., Ltd., Benxi, China), and acclimatized for 7 days in SPF facilities. The IACUC of Jilin University (Approval No. SY202310015) and the Ethics Committee of the First Hospital of Jilin University (Approval No. 24K227-001) formally authorized all experimental procedures. Human participants provided documented informed consent before biospecimen collection.

Primary NSCLC specimens (G0) underwent immediate preservation in antibiotic-supplemented Leibovitz's L-15 (4 °C). Tissue processing was initiated with mechanical fragmentation into 1-mm^3 explants and subcutaneously implanted into the flank region of recipient mice (G1 generation). When G1 xenografts reached approximately 1000 mm^3 (volume calculated as $V = 1/2 \times \text{Length} \times \text{Width}^2$) after 8 weeks, they were excised and serially passaged to establish G2 and G3 generations using identical procedures[38].

At G3 tumor volumes of 100 mm^3, three treatment groups ($n = 6$ per group) were established *via* stratified randomization: PBS, AI-sEVs (2.5 mg/kg), and PD-L1 antibody (10 mg/kg). Freshly isolated human peripheral blood mononuclear cells (Hu-PBMCs from healthy donors) underwent systemic administration *via* tail vein injection (7.5×10^5 cells/mouse) to generate humanized PDX models[39]. Successful immune reconstitution was confirmed 4 weeks post-transplantation by flow cytometry detection of human $CD45^+$ cells. Treatments were administered intravenously every 3 days for 7 cycles, with continuous monitoring of tumor volume and body weight. Following euthanasia, tumors and major organs were harvested for histopathological analysis comparable to orthotopic models.

2.17. *Histopathology, IHC, and tissue immunofluorescence (IF)*

Fresh mouse tissues were fixed in 4% paraformaldehyde (PFA, Sigma−Aldrich, 158127, St. Louis, MO, USA) for 24 h, dehydrated through a graded ethanol series, cleared in xylene, and paraffin-embedded (Paraplast Plus, Leica, Sigma−Aldrich, P3683, St. Louis, MO, USA). Sections (4 μm) were prepared using a rotary microtome (Leica Biosystems, RM2235, Deer Park, IL, USA).

For hematoxylin and eosin (H&E) staining, tissue sections underwent dewaxing and graded alcohol rehydration before staining. Nuclei were visualized with a 5-min hematoxylin immersion, followed by acid-alcohol destaining to achieve specificity. Alkaline bluing was performed under running tap water—cytoplasmic counterstaining employed eosin for 3 min. Finally, slides were dehydrated, cleared in xylene, and coverslipped using mounting medium.

For IHC, sections received microwave antigen retrieval in citrate buffer (pH 6.0, 20 min). Endogenous peroxidase was blocked (3% H_2O_2, 10 min), followed by blocking of non-specific sites (5% normal goat serum, 30 min). Primary antibodies (*e.g.*, Ki67, IL-7) were incubated overnight at 4 °C. After washing, biotinylated secondaries (30 min) and streptavidin-HRP (30 min) were sequentially applied. Signal was developed with DAB, nuclei counterstained with hematoxylin, and slides dehydrated, cleared, and mounted.

Following blocking and washing analogous to IHC (without DAB development), tissue sections received primary antibodies (*e.g.*, LC3, MHC-I) in an overnight incubation (4 °C). Fluorophore-tagged secondary antibodies were then applied for 1 h. Nuclei were labeled with DAPI (5 min). Specimens were mounted in antifade medium and visualized by fluorescence microscopy.

2.18. *Flow cytometry*

Newly excised tumor specimens were mechanically fragmented into small cubes (approximately 1 mm^3) and subsequently subjected to enzymatic digestion within RPMI-1640 medium containing 160 U/mL collagenase IV (Thermo Fisher, 17104019, Waltham, MA, USA) at 37 °C for 30 min with periodic agitation[40]. Following tissue homogenization, cell suspensions were subjected to sequential filtration through 70-μm mesh filters (Corning, 431751, Corning, NY, USA) to isolate single cells and treated with ACK lysing buffer (Thermo Fisher, A1049201, Waltham, MA, USA) to eliminate erythrocytes. Single-cell suspensions were adjusted to 1×10^6 cells/mL in FACS buffer.

To minimize nonspecific binding, cells were pre-blocked with anti-mouse CD16/CD32 antibodies (Clone 93, BioLegend, 101302, San Diego, CA, USA) at a 1:100 dilution on ice for 10 min. Surface marker staining was performed using pre-titrated fluorochrome-conjugated antibodies: Fixable Viability Dye eFluor™ 780 (Invitrogen, 65-0865-14, Carlsbad, CA, USA), anti-CD45-eFluor™ 506 (Clone 30-F11, eBioscience, 69-0451-82, San Diego, CA, USA), anti-CD3-FITC (Clone 17A2, BioLegend, 100204, San Diego, CA, USA), anti-CD4-APC (Clone GK1.5, BioLegend, 100412, San Diego, CA, USA), anti-CD8-PerCP-eFluor™ 710 (Clone 53-6.7, eBioscience, 46-0081-82, San Diego, CA, USA), and anti-Foxp3-PE (Clone FJK-16s, eBioscience, 12-5773-82, San Diego, CA, USA). Cell suspensions were exposed to multicolor antibody mixtures for 30 min under chilled conditions (4 °C) on ice under light-protected conditions, followed by two washes in ice-cold FACS buffer. Stained cells were diluted in 400 μL FACS buffer and analyzed using a Beckman Coulter CytoFLEX LX flow cytometer (Brea, CA, USA), acquiring at least 50,000 live singlets per sample (Supporting Information Fig. S2).

2.19. *ELISA and safety assessment*

Serum samples ($n = 6$ per group) were collected in EDTA-coated vacutainers and centrifuged (3000×*g*, 10 min, 4 °C) to harvest

supernatants. Quantification of target proteins was performed using commercial ELISA kits specific for mouse TNF-α, IFN-γ, IL-2 (Elabscience, Catalog#E-EL-M3063, # E-EL-M0048, #E-EL-M0042, Wuhan, China), and IL-7 (MultiScience, Catalog#EK207/2-AW1, Wuhan, China), following the manufacturer's protocol with slight modifications. Briefly, standards (ranging from 0 to 500/1000 pg/mL) and samples were incubated in pre-coated 96-well plates for 1.5 h at 37 °C. Following five successive washes with the designated cleaning buffer, each well received 100 μL of biotin-conjugated detection antibodies and was incubated for 60 min. Subsequently, streptavidin−HRP conjugate was applied for 30 min. The reaction was visualized using TMB substrate, developed in the dark for 15 min, and terminated with stop solution. Optical density measurements (450 nm/630 nm) were acquired on a BioTek Gen5 absorbance reader (BioTek, Gen5, Winooski, VT, USA).

For safety assessments, peripheral blood was collected in EDTA-coated tubes. Serum levels of alanine aminotransferase (ALT; Catalog#E-BC-K235-M), aspartate aminotransferase (AST; Catalog#E-BC-K236-M), blood urea nitrogen (BUN; Catalog#E-BC-K183-M), and creatinine (Cr; Catalog#E-BC-K188-M) were determined using commercially available assay kits (Elabscience, Wuhan, China), according to the manufacturer's instructions. Absorbance readings were measured at specified wavelengths using the BioTek Gen5 microplate reader.

2.20. Tissue collection and cell suspension preparation

Fresh mouse lung cancer tissues were collected within 30 min post-resection under sterile conditions and immediately immersed in ice-cold tissue preservation solution to preserve cell viability. Tissue specimens were mechanically fragmented into 1−2 mm^3 pieces and enzymatically disaggregated in DMEM/F12 medium containing 10% FBS, supplemented with 1 mg/mL collagenase IV (Worthington Biochemical, V900893, Freehold, Lakewood, NJ, USA) and 20 U/mL hyaluronidase. Digestion was conducted at 37 °C for 30 min under mild agitation. The liberated cell suspension was clarified through a 40-μm strainer, followed by two PBS washing cycles. Cell viability, exceeding 90%, was confirmed using Trypan Blue exclusion on a Countess II FL Automated Cell Counter (Thermo Fisher, Countess™ II FL, Waltham, MA, USA). Single-cell suspensions were adjusted to a concentration of 1000 cells/μL in PBS with 0.04% BSA for downstream processing.

2.21. Single-cell RNA sequencing (scRNA-seq)

Single-cell capture and library generation were performed using Chromium Next GEM Single Cell 3' Reagent Kits v3.1 (10 × Genomics, Pleasanton, CA, USA) on the 10x Genomics Chromium Controller platform, targeting 10,000 cells per sample to ensure comprehensive transcriptome coverage. Cells were lysed in droplets to release RNA, which was reverse-transcribed with template-switching oligos (TSOs) containing unique molecular identifiers (UMIs) to correct for amplification bias. Following reverse transcription, cDNA was amplified through 12 PCR cycles. Subsequent fragmentation and adapter ligation utilized Illumina TruSeq HT chemistry. Final libraries were assessed for concentration (Qubit 4.0 Fluorometer) and size distribution (Agilent 2100 Bioanalyzer, High Sensitivity DNA Kit), with 300−500 bp inserts validated. Paired-end sequencing (2 × 150 bp) was performed on an Illumina NovaSeq 6000 (Illumina, NovaSeq 6000, San Diego, CA, USA), achieving a depth exceeding 50,000 reads per cell to ensure robust gene detection.

2.22. ScRNA-seq data processing and analysis

The raw scRNA-seq data were processed using Cell Ranger (v7.1.0) with alignment to the mm10-2020-A reference genome. Doublets were identified and removed using Scrublet (v0.2.3). Batch effects were corrected using Harmony (v0.1.1). Dimensionality reduction (UMAP) and clustering were conducted in Seurat (v5.0.1), with cell type annotation supported by SingleR (v2.0.0) against the Mouse Cell Atlas. Differentially expressed genes (DEGs) were identified using MAST (v1.24.0) with thresholds of $|\log_2(\text{fold change})| > 0.5$ and adjusted P-value <0.05 (Benjamini−Hochberg correction). Pathway enrichment analysis utilized Gene Ontology (GO) and Reactome databases *via* clusterProfiler (v4.10.0)[41]. Raw data were deposited in NCBI GEO (Accession: GSE298562).

2.23. Cell trajectory analysis

To assess cellular developmental potential, we applied CytoTRACE (v0.3.3), a computational tool that quantifies transcriptional diversity to infer cell potency, assigning a CytoTRACE score to each cell. The cluster with the lowest median CytoTRACE score was selected as the trajectory root. For pseudotime reconstruction, we employed Monocle2 (v2.28.0) using highly variable genes identified by Seurat. Dimensionality reduction was performed *via* the DDRTree algorithm, followed by pseudotemporal ordering of cells. Branch-dependent gene expression dynamics were analyzed using branched expression analysis modeling (BEAM), a statistical framework designed to detect differentially expressed genes across trajectory branches.

2.24. The cancer genome Atlas (TCGA) data analyses

Transcriptomic profiles and associated clinicopathological metadata across 33 distinct tumor types were obtained from TCGA repositories. FPKM-normalized RNA sequencing data (processing level 3) were retrieved for TCGA-LUAD (lung adenocarcinoma) and TCGA-LUSC (lung squamous cell carcinoma) projects (https://portal.gdc.cancer.gov/). Tumor immune scores were derived *via* the ESTIMATE algorithm, which employs non-negative matrix factorization (NMF) to estimate immune cell proportions from bulk RNA-seq data. Single-sample Gene Set Enrichment Analysis (ssGSEA) was subsequently conducted using R packages GSVA (v 1.52.3) in R software (v.4.4.1) and the ssGSEA immuno-infiltration algorithm to quantify infiltration levels of 24 distinct immune cell subtypes. Correlation coefficients (r) derived from Spearman's rank correlation quantified association strengths between variables.

2.25. RNA-seq and transcriptome analysis

Total RNA was extracted from six lung cancer patients who had undergone anti-PD-L1 immunotherapy ($n = 3$ per group) using TRIzol® reagent (Invitrogen, Carlsbad, CA, USA), followed by DNase I treatment (Qiagen) to degrade contaminating genomic DNA before downstream processing. RNA integrity was validated *via* Agilent 2100 Bioanalyzer, ensuring all samples had an RNA Integrity Number (RIN) > 8.0. Total RNA underwent poly (A) + selection *via* magnetic separation with NEBNext® oligo

(dT) beads (New England Biolabs) to isolate mature mRNA transcripts. The enriched mRNA was fragmented at 94 °C for 8 min in a magnesium-based buffer to generate 200−300 bp fragments. First-strand cDNA synthesis was performed using random hexamer primers and SuperScript IV Reverse Transcriptase (Thermo Fisher, Waltham, MA, USA), followed by second-strand synthesis incorporating dUTP to preserve strand specificity. The resulting double-stranded cDNA underwent end-repair using T4 DNA polymerase and Klenow fragment (NEBNext® Ultra II DNA Library Prep Kit), with adenine (A) overhangs added to the 3′ termini using Klenow sEV (3′→5′ sEV minus). Illumina-compatible sequencing adapters (TruSeq Universal Adapters) were ligated to the A-tailed fragments, and unligated adapter dimers were removed *via* AMPure XP bead purification (Beckman Coulter, Brea, CA, USA). Adapter-ligated DNA was amplified through 12 cycles of PCR using indexed primers complementary to the adapter sequences. Final libraries were purified using AMPure XP beads to eliminate primer dimers and residual contaminants.

Raw sequencing data underwent quality control *via* FastQC (v0.11.9) (Andrews, 2010), with adapter trimming and removal of low-quality reads (Phred score <30) performed using fastp (v0.22.0). Clean reads were aligned to the hg19 reference genome using STAR (v2.4.2a) with default parameters. Transcript assembly and quantification were performed *via* RSEM (v1.2.29), with normalization to transcripts per kilobase million (TPM). Differential expression analysis was conducted using edgeR (v3.28.1), applying thresholds of $|\log_2(\text{fold change})| \geq 1$ and an adjusted *P*-value <0.05 (Benjamini−Hochberg correction). Functional enrichment of DEGs was analyzed through GO and Kyoto Encyclopedia of Genes and Genomes (KEGG) pathways using clusterProfiler (v3.14.3). Raw data and processed matrices have been deposited in the NCBI GEO repository (Accession: GSE298789).

2.26. Statistical analysis

All experimental procedures included three or more independent biological replicates. Quantitative outcomes are expressed as mean ± standard deviation (SD). Between-group variations were assessed through two-sample Student's *t*-tests with two-tailed distribution assumptions for pairwise comparisons, one-way analysis of variance (ANOVA) or two-way ANOVA models for multi-group evaluations, supplemented with Tukey's multiple comparisons test where applicable. Statistical significance was defined as $^{*}P < 0.05$, and is denoted as follows: $^{*}P < 0.05$, $^{**}P < 0.01$, $^{***}P < 0.001$, $^{****}P < 0.0001$. All computations were executed using GraphPad Prism 8 (v10.4.0).

3. Results

3.1. Low IL-7 expression in NSCLC tumor tissues correlates with poor prognosis following immunotherapy

To investigate the prognostic relevance of autophagy on immunotherapy outcomes, we analyzed paraffin-embedded tumor biopsy specimens from six NSCLC patients who subsequently underwent anti-PD-L1 neoadjuvant immunotherapy at the Cancer Hospital of the Chinese Academy of Medical Sciences. Differential gene expression analysis identified 788 upregulated and 283 downregulated genes in patients with poor responses compared to those with favorable outcomes based on pathological assessment of surgically resected tumor tissue, as illustrated in the volcano plot (Fig. 2A). GO enrichment analysis indicated that genes associated with extracellular vesicles and immune-related metabolic pathways were predominantly upregulated in better responsive patients (Fig. 2B). Conversely, KEGG pathway analysis of the poorly responsive group showed enrichment in cancer-associated signaling cascades, including PI3K−AKT signaling pathway, chemical carcinogenesis-DNA adducts, extracellular matrix (ECM)−receptor interaction, and NOD-like receptor signaling pathway (Fig. 2C). Among these differentially expressed genes, *IL-7*, a cytokine closely related to autophagy, was significant downregulated in patients with poor immunotherapy outcomes (Supporting Information Table S1).

Analysis of the TCGA database and pathological data confirmed that IL-7 expression is low in both LUAD and LUSC (Fig. 2D and E, Supporting Information Fig. S3). Furthermore, a pan-cancer analysis of 33 tumor types utilizing TCGA data demonstrated that *IL*-7 RNA expression exhibited statistically significant positive correlation with immune scores across nearly all malignancies through Spearman correlation analysis (Supporting Information Fig. S4). In LUAD and LUSC specifically, ssGSEA showed strong correlations between *IL*-7 RNA expression and several immune cell subsets, especially T cells, Th1 cells, and dendritic cells (DCs) (Fig. 2F and G). Notably, *IL-7* levels were positively correlated with $CD8^+$ T cell infiltration and the expression of $CD8^+$ T cell-associated genes, including *CD8A*, *CD8B*, *PRF1*, *GZMA*, *GZMB*, and *GZMK* (Fig. 2H and I, Supporting Information Fig. S5). Altogether, *IL-7* expression was positively correlated with the integral immune infiltration scores of LUAD and LUSC, suggesting that elevated IL-7 expression may promote immune infiltration and anti-tumor immune responses (Fig. 2J and K). To validate these findings, we performed pathological histochemistry, Western blotting, and RT-qPCR analyses, confirming that both mRNA and protein levels of IL-7 were significantly lower in tumor tissues from NSCLC patients with poor responses to anti-PD-L1 therapy compared to those with better clinical outcomes (Fig. 2L−O). In summary, our findings indicate that IL-7 expression is reduced in NSCLC patients with poor immunotherapy prognosis and is positively correlated with immune cell infiltration, suggesting its potential as a target for the improvement of anti-PD-L1 immunotherapy.

3.2. Efficient AI-sEV preparation via DES and characterization

To restore immunotherapy responsiveness in NSCLC patients with poor outcomes, we developed multifunctional AI-sEVs designed to inhibit autophagy and enhance immune responses. These sEVs carry *IL*-7 mRNA and feature anti-PD-L1 antibodies conjugated to their membrane surface. To enable efficient mRNA loading, we developed a DES that integrates ultrasound with nanosecond pulses, transiently permeabilizes cell membranes within a liquid flow to enhance nucleic acid transfection (Fig. 1). Stimulation by the tandem nanosecond pulse-ultrasound jet led to a 30-fold increase in sEV yield in HEK293T and a 24-fold increase in MEF cells compared to conventional method (Fig. 3A and Supporting Information Fig. S6). Electroporation conditions were optimized to balance high sEV yield and transfection efficiency while maintaining cell viability. Adjusting pulse amplitude from 100 to 200 V improved both sEV yield and transfection efficiency, peaking at 160 V, beyond which cell viability declined (Fig. 3B and C, Supporting Information Table S2). Further optimization of pulse frequency (150 kHz) and duration (600 ns) yielded maximal sEV secretion and superior transfection efficiency (Supporting Information Fig. S7, Tables S3 and S4). Additionally, a flow

rate of 2 mL/h was identified as optimal, balancing high transfection efficiency with minimal impact on cell viability (Supporting Information Fig. S8, Tables S5 and S6). Similar optimization in MEF cells yielded consistent results (Supporting Information Fig. S9, Table S7−S9). Morphological analysis confirmed the structural integrity of DES-generated sEVs, which were comparable in size and appearance to PBS-treated controls (Supporting Information Fig. S10). Notably, *IL-7* mRNA content in DES-treated sEVs was over 3500 times higher than in control groups (Fig. 3D), demonstrating that DES technology not only

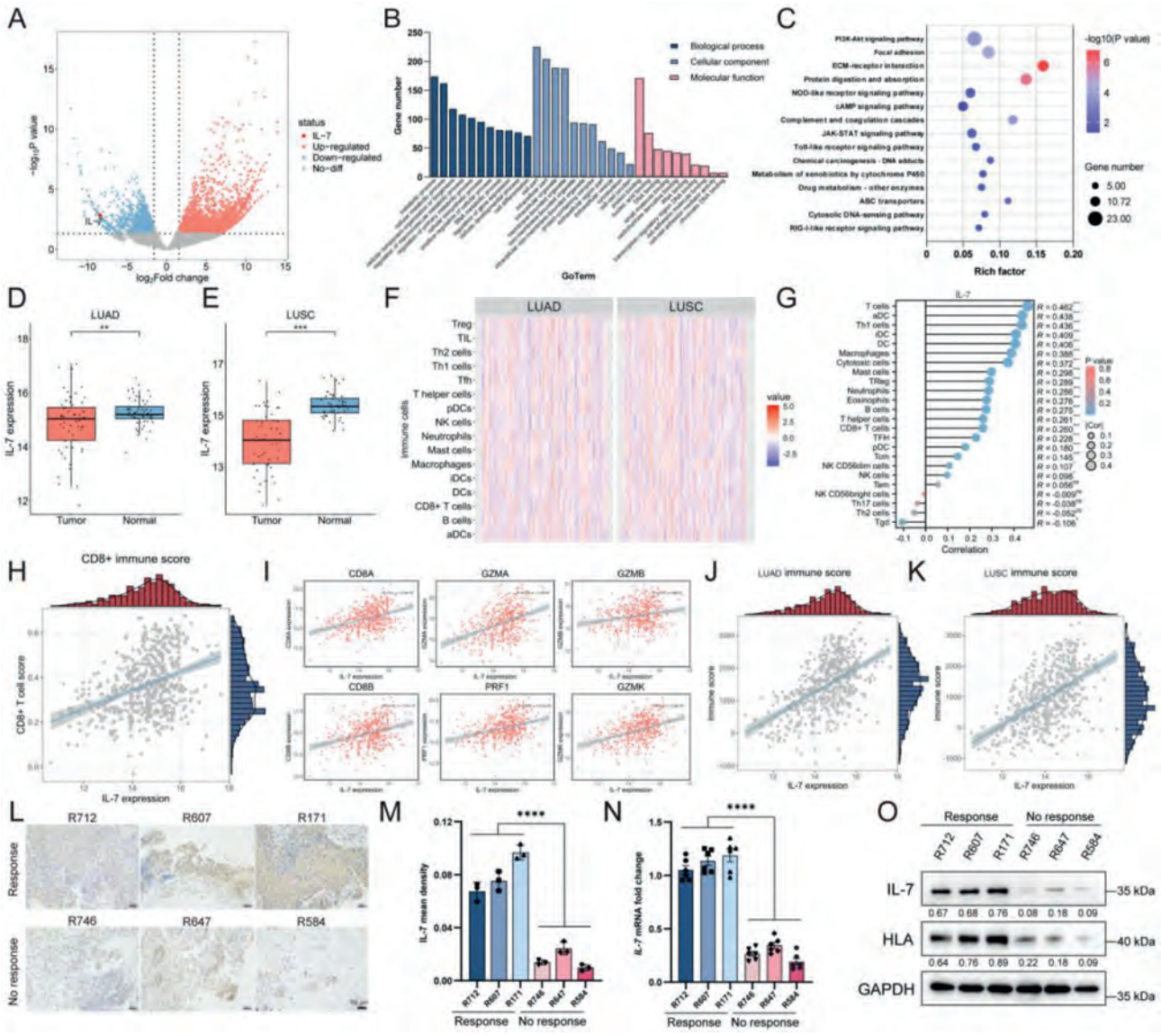

Figure 2 Low IL-7 expression in NSCLC tumor tissues correlates with poor immunotherapy prognosis. (A) Transcriptome volcano plot showing differentially expressed genes between NSCLC patients with good *versus* poor responses to PD-L1 immunotherapy. Red and blue dots represent significantly upregulated and downregulated genes, respectively. (B) GO enrichment analysis of differentially expressed genes with different prognostic effects after immunotherapy. (C) KEGG pathway enrichment analysis of differentially expressed genes related to immunotherapy outcomes. IL-7 expression levels in (D) LUAD and (E) LUSC tumor samples compared to matched adjacent normal tissues. (F) Heatmap showing *IL-7* mRNA-correlated immune cell infiltration across 16 immune cell types in LUAD and LUSC, calculated using ssGSEA. (G) Correlation of IL-7 expression with infiltration levels of 24 immune cell types in NSCLC based on the TCGA database. (H) Correlation between IL-7 expression and activated $CD8^+$ T cell scores in LUAD. (I) Scatter plot showing correlations between IL-7 expression and $CD8^+$ T activation markers (*CD8A*, *GZMA*, *GZMB*, *CD8B*, *PRF1*, and *GZMK*) in 574 LUAD samples ($\log_2$(FPKM+1)). Correlation between *IL-7* expression and stromal scores in (J) LUAD and (K) LUSC based on TCGA datasets. (L) Representative IHC images showing IL-7 protein expression in NSCLC tumor tissues from patients with distinct immunotherapy prognoses. Scale bar: 50 μm. (M) Quantitative analysis of IL-7 protein expression in tumor tissue sections stratified by treatment response. (N) RT-qPCR analysis of *IL-7* mRNA expression in the same cohort. (O) Western blot analysis of IL-7 and HLA expression in NSCLC tumor tissues from patients treated with PD-L1 immunotherapy. Two-tailed Spearman correlation analysis was performed in (G−K). Data in (M) and (N) are illustrated as mean ± SD ($n = 3$ per group). Statistical significance was calculated by Student's *t*-test or one-way ANOVA followed by Tukey's multiple comparisons test. $^*P < 0.05$, $^{**}P < 0.01$, $^{***}P < 0.001$, $^{****}P < 0.0001$.

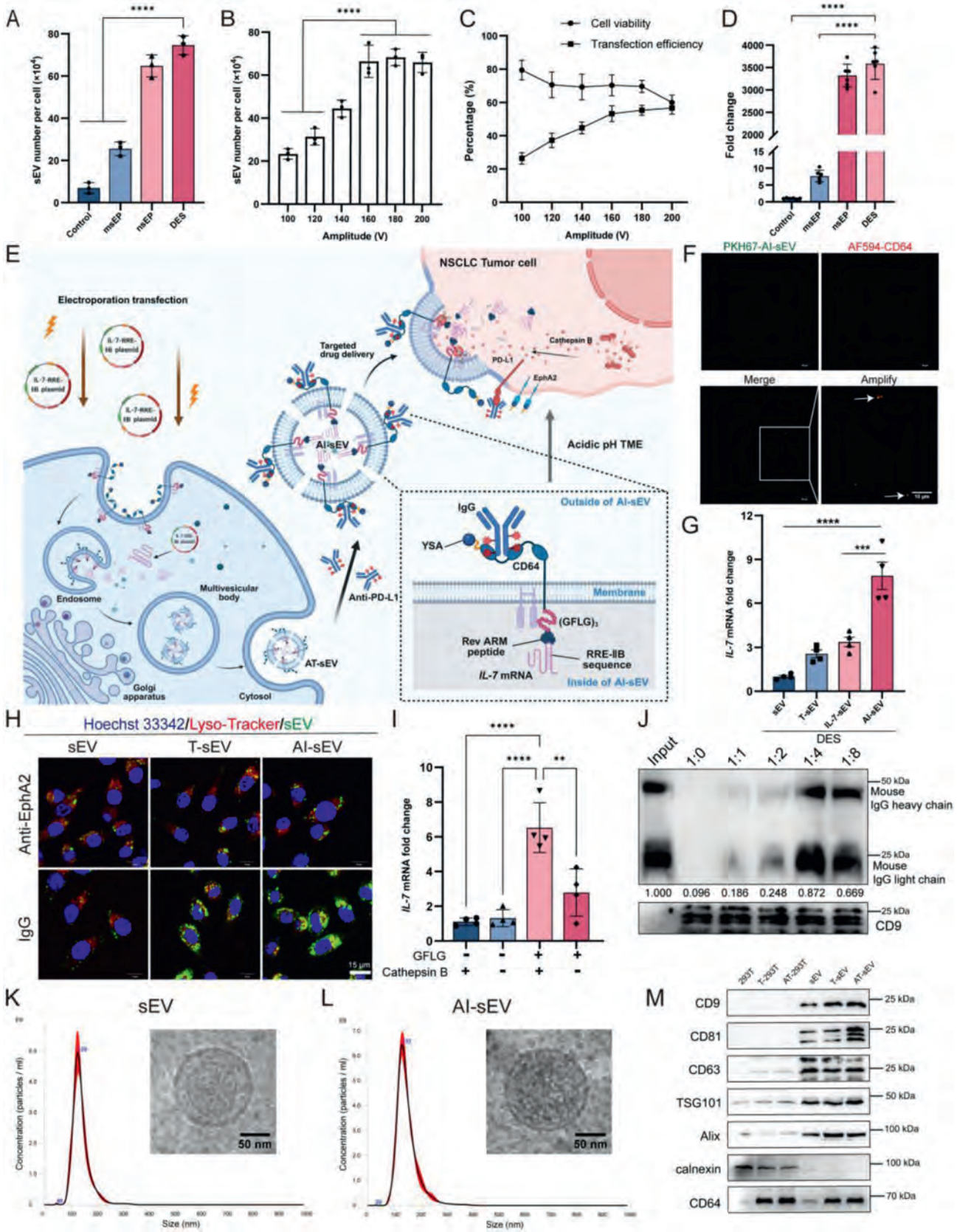

Figure 3 Efficient preparation of AI-sEV *via* DES and characterization. (A) Quantification of sEVs production per HEK293T cell across different treatment groups: untreated control, millisecond electroporation (msEP), nanosecond electroporation (nsEP), and DES. (B) sEV yield per HEK293T cell after DES treatment across voltage amplitudes ranging from 100 to 200 V. (C) Assessment of cell viability and transfection efficiency of HEK293T cells following DES treatment at different voltage amplitudes. (D) RT-qPCR analysis of *IL-7* mRNA levels in sEVs, showing a significantly higher

enhances functional sEV production but also significantly increases sEV mRNA loading efficiency.

We further developed a versatile sEV engineering strategy to support delivery of both nucleic acids and protein therapeutics (Fig. 3E). To enable antibody loading, HEK293T/MEF cells were engineered to express CD64 stably, leveraging its role as a transmembrane glycoprotein and high-affinity IgG Fc receptor to allow specific binding to anti-PD-L1 antibodies (Supporting Information Fig. S11). IF imaging confirmed co-localization of EGFP-CD64 with the sEV marker CD63 in both HEK293T cells and their secreted sEVs, indicating that CD64 is predominantly expressed on the membrane of sEVs (Fig. 3F and Supporting Information Fig. S12). To enhance *IL*-7 mRNA loading efficiency, we employed a Rev-Rev response element (RRE) system: the arginine-rich motif (ARM) of Rev protein (Rev ARM peptide) was fused to the CD64 C-terminus, and a non-functional RRE-IIB sequence was appended to the 3′ end of *IL*-7 mRNA. This resulted in a further 8-fold increase in *IL*-7 mRNA loading within the sEVs, without affecting housekeeping gene expression (Fig. 3G). Furthermore, confocal imaging confirmed the successful loading of *IL*-7 mRNA into sEVs (Supporting Information Fig. S13). Quantitative analysis further revealed an average of approximately 178.97 *IL*-7 mRNA copies per 100 sEVs (Supporting Information Fig. S14). To enable targeted delivery to NSCLC cells, a 12-amino acid YSA peptide—specific for the EphA2 receptor, which is overexpressed in NSCLC—was fused to the N-terminus of CD64. Competitive binding assays with an anti-EphA2 antibody significantly reduced the cellular uptake of sEVs in both tested cell lines, confirming EphA2-specific targeting. Notably, no significant difference in fluorescence intensity was observed between T-sEVs lacking anti-PD-L1 antibody and AI-sEVs co-modified with YSA and anti-PD-L1, indicating that the functional integrity of the YSA peptide was not compromised by spatial interference from the conjugated antibody (Fig. 3H and Supporting Information Fig. S15). To enable efficient release of *IL*-7 mRNA within tumor cells, a cathepsin B-cleavable peptide linker $(GFLG)_3$ was inserted between CD64 and Rev ARM peptide. Cathepsin B, activated in the acidic TME, cleaves the phenylalanine—leucine bond, ensuring controlled mRNA release (Fig. 3I). For immune checkpoint blockade, anti-PD-L1 antibodies were conjugated to CD64 on the AI-sEV surface. Optimal binding was observed at an sEV protein-to-antibody (*w*/*w*) ratio of 1:4 (Fig. 3J and Supporting Information Fig. S16). Western blot analysis revealed that the average loading capacity of anti-PD-L1 antibody was 86.6 ± 9.2 ng per μg of sEV protein, confirming the efficient surface conjugation of antibodies on AI-sEVs for targeted immunotherapy (Fig. 3J). To assess binding stability and release behavior under TME conditions, parallel release experiments were conducted at physiological (pH 7.4) and acidic (pH 6.5) conditions, mimicking the TME. The AI-sEVs/anti-PD-L1 conjugate exhibited high stability at pH 7.4, while a significant and time-dependent release of the antibody was observed at pH 6.5, with nearly complete release within 24 h (Supporting Information Fig. S17). This confirms the pH-sensitive release profile of the antibody from AI-sEVs, supporting their potential for targeted delivery and activation within the TME.

Cryo-TEM imaging confirmed that AI-sEVs retained typical bilayer vesicle structures with particle sizes above 100 nm (Fig. 3K and L). NTA further revealed an average particle size of 140.2 ± 33.8 nm for control sEVs and 149.7 ± 41.4 nm for AI-sEVs, indicating antibody conjugation (Fig. 3K and L). ξ-potential measurements showed a surface charge shift from −4.8 ± 0.86 mV in control sEVs to −9.42 ± 1.11 mV in AI-sEVs, suggesting successful surface functionalization (Supporting Information Fig. S18). Western blot analysis confirmed enrichment of canonical sEV markers, including CD9, CD81, CD63, and ESCRT-associated proteins (TSG101 and Alix), and absence of the ER protein calnexin, indicating high purity (Fig. 3M and Supporting Information Fig. S19). Additionally, DES-generated sEVs from both HEK293T and MEF cells exhibited high expression levels of CD64 (Fig. 3M and Fig. S19), confirming the successful incorporation of these functional components.

To ensure the feasibility of AI-sEVs for clinical application, we conducted a comprehensive biosafety evaluation. Hemolysis assays demonstrated no significant hemolysis, even at a 10-fold concentration (Supporting Information Fig. S20), suggesting excellent hemocompatibility. Furthermore, cytotoxicity assays confirmed that AI-sEVs exhibit high biocompatibility (Supporting Information Fig. S21), reinforcing their potential as a safe and effective therapeutic platform.

3.3. AI-sEVs inhibit autophagy and promote MHC-I expression in vitro

To investigate the therapeutic potential of AI-sEVs in NSCLC, we first assessed the expression levels of EphA2, PD-L1, and autophagy-related proteins (Beclin-1, ATG7, and IL-7) across multiple lung cancer cell lines. Based on their high receptor levels, low IL-7 expression, and elevated autophagy activity, A549 and LLC cells were selected for further studies (Supporting Information Fig. S22). Flow cytometry analysis revealed time-dependent uptake of AI-sEVs by NSCLC cells, with

IL-7 mRNA loading in sEVs generated by DES treatment compared to other methods. (E) Schematic representation of the AI-sEV construction, designed as an active platform for nucleic acids and protein delivery. (F) Confocal imaging of PKH67-labeled AI-sEV (green) expressing AF594-CD64 (red), confirming CD64 localization on sEV membranes. Scale bar: 10 μm. (G) RT-qPCR quantification of *IL*-7 mRNA in sEVs, demonstrating the enhancement in mRNA loading *via* Rev ARM peptide—*RRE-IIB-IL*-7 mRNA interactions. *U6* was used as an internal standard. (H) Confocal imaging of cellular uptake of sEV, lung tumor-targeted sEV (T-sEV), and AI-sEVs (green) by A549 cells, with or without IgG or anti-EphA2 pretreatment, to evaluate the targeting ability of the YSA peptide. Scale bar: 15 μm. (I) RT-qPCR quantification of *IL*-7 mRNA in response to Cathepsin B. Following Cathepsin B treatment, the $(GFLG)_3$ peptide bond breaks and releases *IL*-7 mRNA. (J) Optimization of the sEV to antibody ratio by incubating autophagy-targeted sEV (AT-sEV) with anti-PD-L1 antibody for 4 h, followed by Western blot assay to determine the highest binding efficiency. Band intensities were quantified using ImageJ software, and the expression of each protein was normalized to the corresponding input IgG signal. NTA and cryo-TEM images of (K) sEV and (L) AI-sEV demonstrating particle size distribution and their bilayer vesicle structure. Scale bar: 50 nm. (M) Western blot analysis of sEV proteins, including transmembrane markers (CD9, CD81, and CD63), ESCRT-associated proteins (TSG101 and Alix), endoplasmic reticulum protein calnexin (negative control), and stably overexpressed CD64 protein from HEK293T cell lysates and sEVs. Data in (A—D), (G), and (I) are illustrated as mean ± SD ($n = 3$ per group). Statistical significance was calculated by Student's *t*-test and one-way ANOVA with Tukey's multiple comparisons test. *$P < 0.05$, **$P < 0.01$, ***$P < 0.001$, ****$P < 0.0001$.

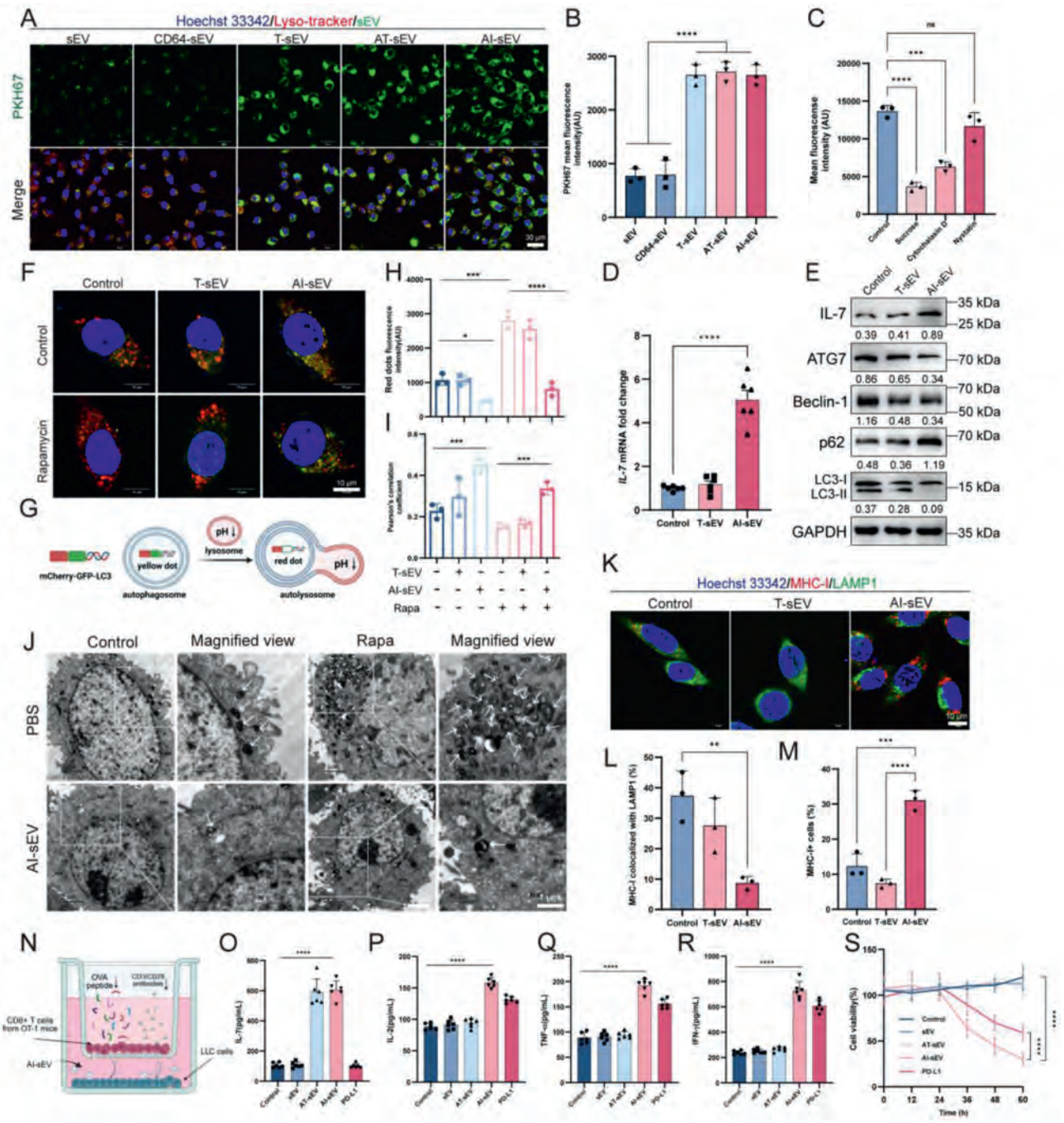

Figure 4 AI-sEVs effectively inhibit autophagy and restore MHC-I expression. (A) Confocal images showing sEV uptake by A549 after 4 h incubation. Scale bar: 30 μm. (B) Quantitative analysis of the average fluorescence intensity of the PKH67-AI-sEVs. (C) Flow cytometry analysis of PKH26-labeled sEV uptake following treatment with inhibitors of specific endocytic pathways: sucrose (0.4 mol/L, clathrin-dependent endocytosis inhibitor), cytochalasin D (5 μmol/L, macropinocytosis inhibitor), and nystatin (50 μmol/L, lipid raft inhibitor). (D) RT-qPCR quantification of intracellular *IL-7* mRNA levels following treatment with T-sEVs and AI-sEVs. (E) Western blot analysis of IL-7 and autophagy-associated proteins (ATG7, Beclin-1, p62, and LC3) in A549 cells treated with PBS, T-sEVs, or AI-sEVs. (F) Confocal imaging of LC3 constructs expressing tandem mRFP-EGFP tags to validate inhibition of autophagy by AI-sEV. Cell nuclei were stained with Hoechst 33342. Scale bar: 10 μm. (G) Schematic representation of the fluorescent expression profile of LC3 constructs expressing tandem mRFP-EGFP tags in cells. (H) Quantitative analysis of the average fluorescence intensity of the red dot. (I) Quantification of Pearson's correlation coefficient for co-localized yellow fluorescence. (J) TEM images illustrating ultrastructural differences in rapamycin pretreated and untreated A549 cells following exposure to rapamycin and/or AI-sEVs for 24 h. Scale bar: 1 μm. (K) Confocal imaging of MHC-I (red) co-localized with LAMP-positive lysosomes (green). Scale bar:10 μm. (L) Quantitative analysis of MHC-I co-localization with LAMP1. (M) Flow cytometry analysis of MHC-I expression in A549 cells following treatment with T-sEV or AI-sEV. (N) Schematic representation of AI-sEV *in vitro* stimulation of $CD8^+$ T cells to kill LLC cells. ELISA quantification of (O) IL-7, (P) IL-2, (Q) TNF-α, and (R) IFN-γ cytokines in cell supernatants ($n = 6$). (S) Tumor

significantly higher internalization compared to sEVs and T-sEVs, indicating the efficacy of YSA-mediated targeting (Supporting Information Fig. S23A−S23D). CLSM further validated these findings, showing cytoplasmic localization of internalized AI-sEVs (Fig. 4A and B, Fig. S23E). Uptake mechanism studies using co-localization assays and pathway-specific inhibitors demonstrated that clathrin-dependent endocytosis was the predominant internalization route, as evidenced by the marked reduction in uptake upon sucrose treatment (Fig. 4C and Supporting Information Fig. S24).

Following internalization, *IL*-7 mRNA and protein levels increased significantly in NSCLC cells treated with AI-sEVs (Fig. 4D and E), resulting in autophagy suppression. AI-sEV-treated cells exhibited reduced conversion of LC3-I to LC3-II, indicating impaired autophagic flux. Further analysis using an mRFP-EGFP-LC3B tandem reporter allowed visualization of autophagosomes and autolysosomes. Rapamycin, an autophagy inducer, markedly elevated red dot counts as quantified by mRFP-GFP-LC3 fluorescence, demonstrating enhanced autolysosome formation and sustained flux progression. In contrast, AI-sEVs treatment substantially attenuated acidic autolysosomes generation, characterized by a 55.4% reduction in red puncta coupled with increased co-localization coefficients (Pearson's *r*: 0.22 *vs* 0.45), suggesting that autophagic flow was blocked. Although rapamycin co-administration partially rescued autophagic flux parameters, the dominant inhibitory profile of AI-sEVs persisted across all quantitative metrics (Fig. 4F−I and Supporting Information Fig. S25). These findings were corroborated by TEM imaging, which showed a decrease in autophagosome accumulation in AI-sEV-treated A549 cells, compared to rapamycin-pretreated controls (Fig. 4J). Consistent with autophagy inhibition, p62—a substrate that accumulates when autophagy is blocked[42]—was significantly upregulated. At the same time, LC3-II, Beclin-1, and ATG7 were downregulated (Fig. 4E). Moreover, AI-sEV treatment upregulated PI3K, *p*-AKT, and *p*-mTOR, and downregulated *p*-AMPK levels (Supporting Information Fig. S26), suggesting PI3K/AKT/mTOR axis and AMPK signaling as key regulators of autophagy dynamics. Utilizing inhibitors targeting key proteins within these pathways—such as LY294002 (a PI3K inhibitor), rapamycin (an mTOR inhibitor), and compound C (an AMPK inhibitor)—we confirmed that IL-7 activates the PI3K/AKT/mTOR axis while inhibiting the AMPK/mTOR axis, which in turn leads to the suppression of Beclin-1 protein and inhibition of the autophagy process. Furthermore, we employed an IL-7 receptor (IL-7R) neutralizing antibody to block the interaction between IL-7 and IL-7R specifically. Western blot analysis demonstrated that the inhibitory effect on autophagy was significantly reversed when the IL-7R neutralizing antibody or the PI3K inhibitor LY294002 was administered in combination with AI-sEV treatment. In addition, the activation levels of the PI3K/AKT/mTOR pathway and AMPK signaling were markedly reduced. These findings provide direct evidence that the interaction between IL-7 and IL-7R is responsible for the suppression of autophagy and the regulation of downstream signaling pathways (Supporting Information Fig. S27). Together, these results demonstrate that AI-sEVs effectively deliver IL-7 to NSCLC cells, inhibit autophagy through PI3K/AKT/mTOR and AMPK signaling.

Having established the regulatory role of IL-7 in autophagy inhibition, we next examined how this process influences the immunogenicity of NSCLC cells. RT-qPCR and Western blot analyses demonstrated that AI-sEV treatment significantly increased the expression of MHC-I (also known as HLA in human) (Supporting Information Fig. S28), consistent with previous findings that autophagy inhibition can restore MHC-I expression[43]. Confocal microscopy further demonstrated that in untreated LLC and A549 cells, MHC-I was predominantly co-localized with lysosomes and LC3-positive autophagosomes, suggesting lysosome-mediated degradation of MHC-I. In contrast, AI-sEV treatment markedly reduced this co-localization, promoting redistribution of MHC-I to the cell surface (Fig. 4K and L, Supporting Information Fig. S29). Flow cytometry confirmed a significant increase in the proportion of MHC-I$^+$ cells following AI-sEV treatment, underscoring their potential role in enhancing antigen presentation (Fig. 4M). To evaluate the functional impact of AI-sEVs on antitumor immune responses, we co-cultured NSCLC cells with CD8$^+$ T cells previously activated using CD3/CD28 antibodies and the OVA peptide (Fig. 4N). ELISA measurements of the culture supernatants revealed significantly elevated levels of IL-7 and CD8$^+$ T cell-derived cytokines, including IL-2, TNF-α, and IFN-γ in the AI-sEV-treated group (Fig. 4O−R). These responses surpassed those observed with anti-PD-L1 treatment alone. This heightened immune activation was accompanied by a significant reduction in tumor cell viability, indicating that AI-sEVs potentiate CD8$^+$ T cell-mediated cytotoxicity (Fig. 4S). In addition, we compared AI-sEVs with lipid nanoparticles (LNP) co-loaded with *IL*-7 mRNA and anti-PD-L1 antibodies (PI-LNP). The results showed that both delivery systems exhibit good biosafety. However, AI-sEVs demonstrated superior drug delivery efficiency. Furthermore, analysis of *IL*-7 mRNA expression levels and flow cytometry assessment of MHC-I expression confirmed that AI-sEVs achieved better therapeutic efficacy compared to PI-LNPs (Supporting Information Fig. S30). In conclusion, AI-sEVs are efficiently internalized by NSCLC cells, where they inhibit autophagy *via* activation of the PI3K/AKT/mTOR axis. This inhibition prevents MHC-I degradation through lysosomal mechanisms, thereby enhancing antigen presentation, promoting NSCLC immunogenicity, and facilitating robust T cell-mediated tumor cell killing *in vitro*.

3.4. AI-sEVs inhibit tumor growth and suppress autophagy in an orthotopic NSCLC model

To evaluate the therapeutic potential of AI-sEVs *in vivo*, we established an orthotopic LLC model in C57BL/6 mice to assess their immunotherapeutic effects (Fig. 5A). Biodistribution analysis *via* IVIS imaging confirmed that AI-sEVs, modified with targeted peptides, efficiently accumulated in lung tissues, whereas non-targeted sEVs displayed minimal pulmonary localization (Fig. 5B−D). Apart from the expected prominent accumulation in the liver, negligible uptake was observed in other major organs evaluated. Following successful NSCLC model

cell survival was measured using the MTS assay ($n = 3$). Data in (B−D), (H), (I), (L), (M), (O−S) are illustrated as mean ± SD ($n = 3$ per group). Statistical significance was calculated using Student's *t*-test and one-way ANOVA with Tukey's multiple comparisons test. ns, not significant, $^*P < 0.05$, $^{**}P < 0.01$, $^{***}P < 0.001$, $^{****}P < 0.0001$.

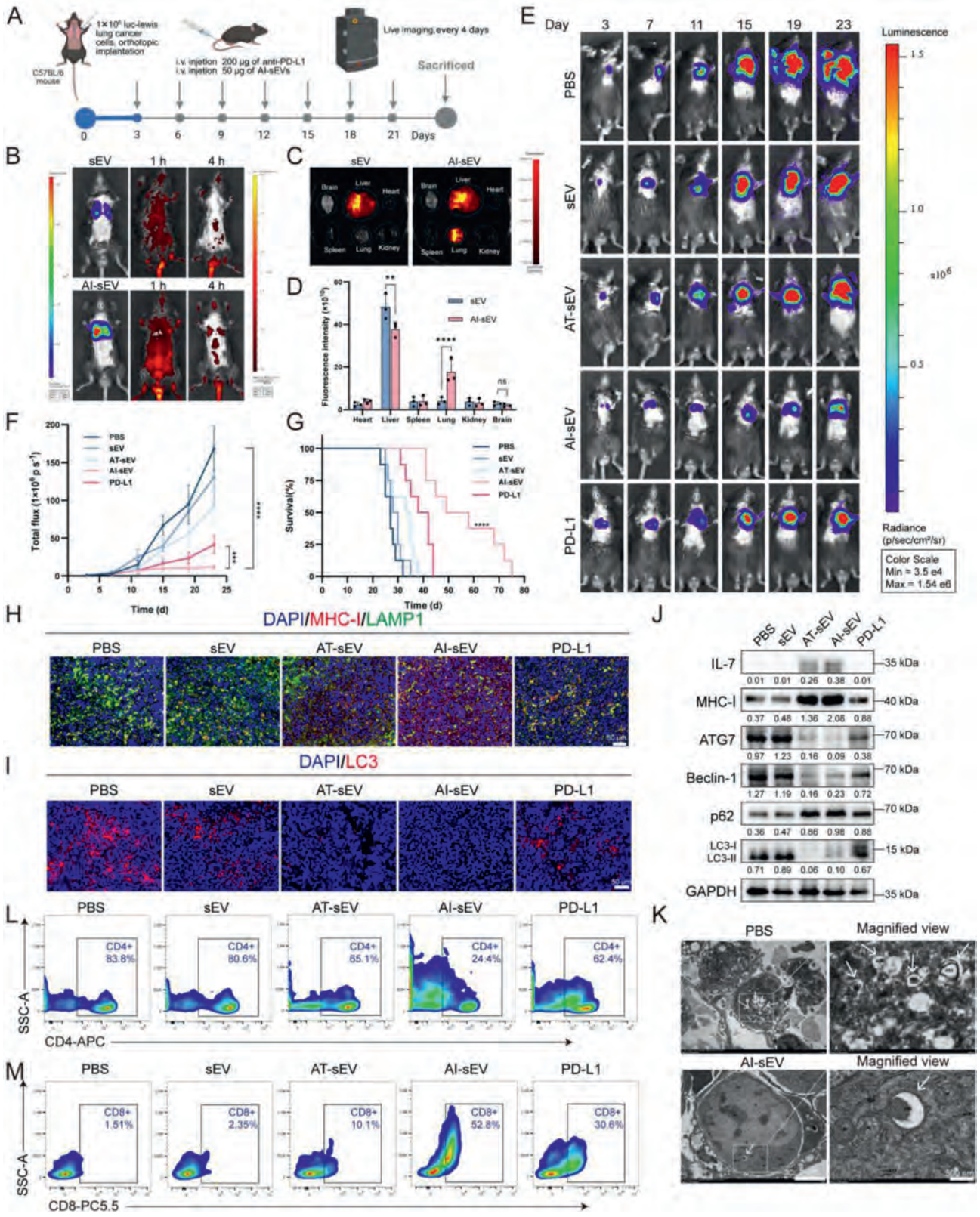

Figure 5 AI-sEVs inhibit tumor growth and suppress autophagy in an orthotopic NSCLC model. (A) Schematic illustration of AI-sEVs treatment in the orthotopic NSCLC model. (B) *In vivo* IVIS imaging showing the preferential accumulation of pKH26-labeled AI-sEVs within orthotopically implanted NSCLC tumors. (C) Tissue distribution analysis confirming high fluorescence intensity in tumor tissue, indicating efficient targeting. (D) Quantitative fluorescence analysis of isolated major organs ($n = 3$). Luminescence imaging of luciferase-labeled tumors *via* IVIS to evaluate (E) tumor size, and corresponding tumor growth profiles based on (F) luminescence intensity ($n = 6$). (G) Kaplan−Meier survival curve analysis of C57BL/6 mice with orthotopic NSCLC following different treatments ($n = 8$). (H) Co-staining IF of

establishment, mice were randomly divided into five treatment groups—saline, anti-PD-L1, sEVs, AT-sEVs, or AI-sEVs—and received administrations every three days for 21 days. Among all groups, AI-sEVs treatment (50 μg EV protein per injection) yielded the most significant tumor suppression (Fig. 5E and F, Supporting Information Fig. S31) and conferred the longest survival benefit (AI-sEVs: 75 days *vs* PBS: 32 days; PD-L1: 47 days; sEVs: 35 days; AT-sEVs: 38 days) (Fig. 5G). Histopathological analysis by H&E staining revealed extensive tumor necrosis and disrupted lung architecture in the model group, whereas the AI-sEV group maintained normal lung histology with minimal necrosis (Supporting Information Fig. S32). Immunohistochemical staining for Ki67 demonstrated markedly reduced proliferation in AI-sEV-treated tumors, whereas high Ki67 expression persisted in other groups, particularly sEVs and AT-sEVs (Fig. S32), indicating ongoing tumor growth.

To investigate whether *IL*-7 mRNA delivered by AI-sEVs modulates autophagy and restores MHC-I expression *in vivo*, we conducted IHC, IF and flow cytometry. Both AI-sEV and AT-sEV treatments significantly upregulated IL-7 and MHC-I expression in tumor tissues (Fig. 5H and Fig. S32), with flow cytometry confirming an increased proportion of MHC-I$^+$ cells, most prominently in the AI-sEV group (Supporting Information Fig. S33). To further elucidate the underlying mechanisms, we evaluated autophagy-related markers and associated signaling pathways. LC3 expression in tumor tissues was significantly reduced after AI-sEV and AT-sEV treatment (Fig. 5I). Meanwhile, AI-sEV treatment resulted in a significant reduction in LC3II/I, Beclin-1, ATG7, and *p*-AMPK levels, while the autophagy inhibition pathway markers p62, PI3K, *p*-AKT, and *p*-mTOR were significantly upregulated, indicative of PI3K/AKT/mTOR-mediated autophagy suppression (Fig. 5J and Supporting Information Fig. S34). TEM corroborated these findings, showing a significant reduction in autophagosome formation in the AI-sEV-treated group compared to the PBS group (Fig. 5K). Immune profiling revealed that AI-sEV treatment significantly increased CD8$^+$ T cell infiltration within lung tumors and spleens, accompanied by a relative decrease in CD4$^+$ T cell populations (Fig. 5L and M, Supporting Information Fig. S35). Furthermore, flow cytometric analysis of immunological memory T cells revealed that AI-sEV treatment significantly reduced the proportion of naïve T cells in the spleen while increasing the population of effector memory T cells. These findings indicate that AI-sEVs can induce durable anti-tumor immunity (Supporting Information Fig. S36). Serum cytokine analysis further demonstrated enhanced cytokine secretion and enhanced T cell activation in the AI-sEV group (Supporting Information Fig. S37), highlighting robust systemic antitumor immunity.

Importantly, AI-sEVs exhibited an excellent safety profile. No significant changes in body weight or histopathological abnormalities were observed in major organs (brain, heart, spleen, livers, and kidneys) following intravenous administration (Supporting Information Fig. S38). Additionally, serum levels of hepatic ALT, AST, BUN, and Cr function markers remained within normal ranges across all treatment groups (Supporting Information Fig. S39). In summary, AI-sEVs demonstrate potent anti-tumor efficacy and safety in an orthotopic NSCLC model. By efficiently delivering *IL*-7 mRNA, AI-sEVs inhibit autophagy, restore MHC-I expression, and activate robust CD8$^+$ T cell responses, culminating in significant tumor regression and prolonged survival.

3.5. AI-sEVs promote cytotoxic and effector T cell activation

To investigate the immunomodulatory effects of AI-sEVs on the TME at single-cell resolution, we performed scRNA-seq on tumor-infiltrating CD45$^+$ immune cells from NSCLC-bearing mice treated with PBS (model), anti-PD-L1, and AI-sEVs (Fig. 6A). A total of ∼30,000 single cells were analyzed (PBS: 9468; anti-PD-L1: 9815; AI-sEVs: 10,510; $n = 3$ mice per group). T-distributed stochastic neighbor embedding (T-SNE) analysis identified 26 distinct cell clusters, including 11 major immune cell types: T cells, natural killer (NK) cells, NKT cells, B cells, neutrophils, macrophages, monocytes, alveolar-macrophages, DCs, mast cells, and plasma cells (Fig. 6B and C, Supporting Information Fig. S40). AI-sEV significantly reshaped the immune landscape, notably increasing the abundance of lymphocytes, including T cells, NK/NKT cells, and B cells (Fig. 6D and E). Further sub-clustering of T, B, and NK cells revealed pronounced changes in the AI-sEV-treated group (Fig. 6F). T cell subtyping revealed six distinct subsets: naïve T cells (*Ccr7*, *Lef1* and *Sell*), proliferating T cells (*Mki67*, *Top2A* and *Stmn1*), cytotoxic T cells (*Gzma*, *Gzmb* and *Ncr1*), immature T cells (*Sox4*, *Rag1* and *Tcf7*), exhausted T cells (*Lag3*, *Ctla4*, *Havcr2* and *Tigit*), and effector T cells (*Tnf* and *Ifng*) (Fig. 6G, Supporting Information Fig. S41A and S41B). AI-sEVs markedly increased the proportion of cytotoxic and effector T cells compared to anti-PD-L1 treatment (Fig. 6H and I), suggesting enhanced activation of tumor-infiltrating cytotoxic lymphocytes and immunogenic remodeling of the TME. Differential gene expression analysis confirmed significant upregulation of *Gzma* and *Gzmb* in cytotoxic T cells, as well as *TNF* and *IFN-γ* in effector T cells (Fig. 6J), indicating enhanced T cell-mediated tumor cytotoxicity. Interestingly, while exhausted T cells were also enriched in the AI-sEV group, these cells expressed high levels of co-stimulatory molecules (*Tnfrsf9* and *Tnfrsf4*) and chemokines (*Ccl3* and *Ccl4*), suggesting a dual phenotype with both effector and immunomodulatory roles (Fig. S41C). This subset may contribute to T cell activation while facilitating recruitment of macrophages, DCs, and NK cells into the TME *via* chemokine signaling. Notably, naïve and immature T cells accounted for ∼60% of the total T cell population in control groups. Still, they were reduced to ∼20% in AI-sEV-treated samples, indicating a shift toward a more differentiated, effector-dominant T cell population (Fig. 6I). KEGG pathway enrichment analysis indicated upregulation of immune-related pathways (*e.g.*, PD-L1 expression and PD-1 checkpoint pathway in cancer, Th1 and Th2 cell differentiation, Th17 cell

MHC-I (red) and LAMP1(green) in tumor tissues. Scale bar: 50 μm. (I) IF staining of LC3 in tumor tissue. Scale bar: 50 μm. (J) Western blot analysis of IL-7, MHC-I, autophagy-associated proteins (ATG7, Beclin-1, p62, and LC3) in tumor tissues. (K) TEM images illustrating ultrastructural differences in AI-sEV-treated or non-treated lung cancer tissues. Scale bar: 500 nm. Representative flow cytometry plots of (L) CD4$^+$ T cells and (M) CD8$^+$ T cells (gated on CD3$^+$ cells) within tumors following different treatments. Data in (D) and (F) are illustrated as mean ± SD. Statistical significance was calculated using Student's *t*-test and one-way ANOVA with Tukey's multiple comparisons test. ns, not significant, $^*P < 0.05$, $^{**}P < 0.01$, $^{***}P < 0.001$, $^{****}P < 0.0001$.

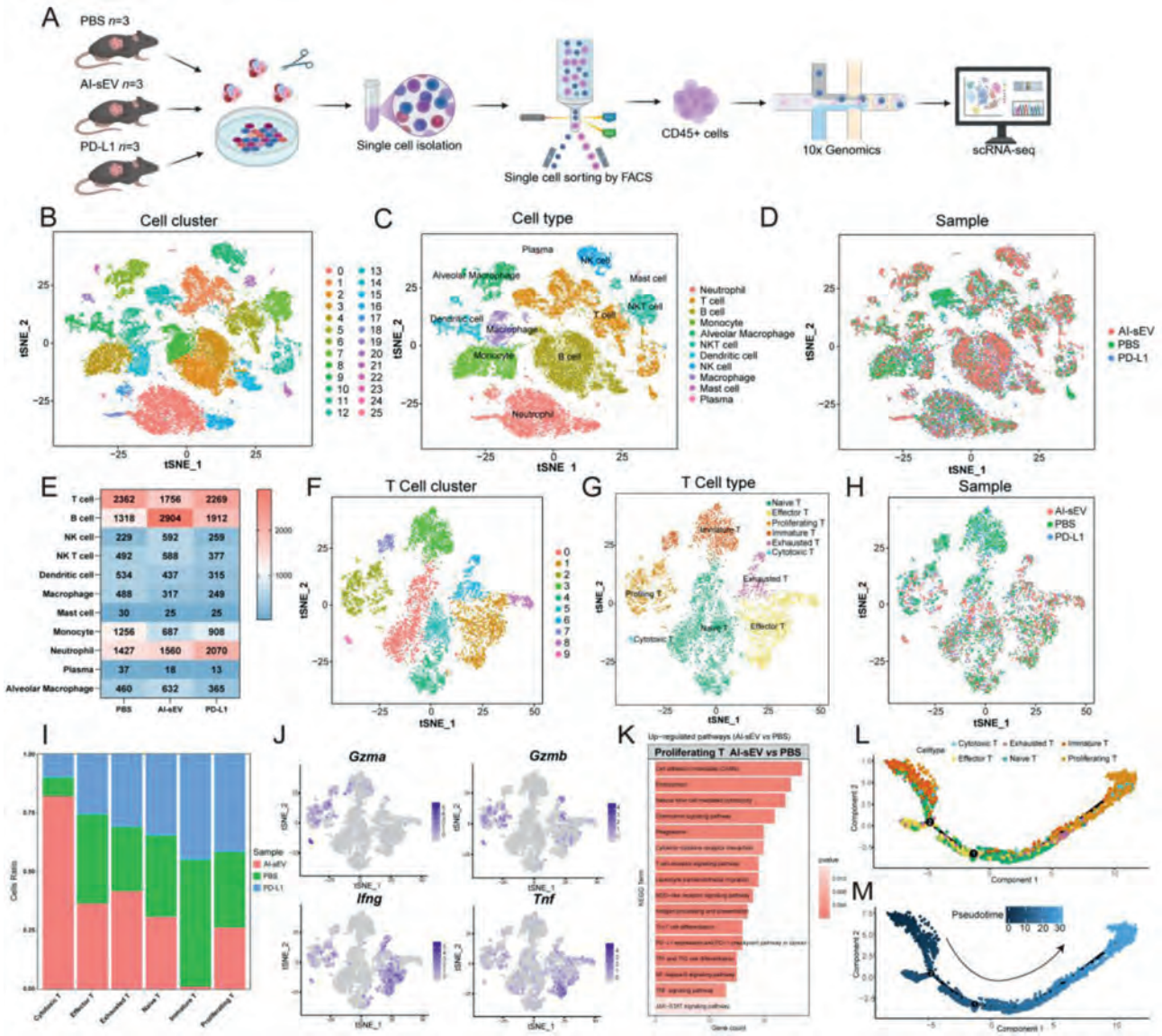

Figure 6 ScRNA-seq analysis reveals AI-sEVs promote cytotoxic and effector T cell activation. (A) Schematic diagram illustrating the experimental workflow for scRNA-seq analysis. T-SNE plots of 29,793 $CD45^{+}$ immune cells isolated from lung cancer tissues of PBS ($n = 3$ biologically independent samples), PD-L1 ($n = 3$ biologically independent samples), and AI-sEV-treated groups ($n = 3$ biologically independent samples). Cells are color-coded according to (B) cell cluster, (C) cell types, and (D) sample groups. (E) Heatmap showing the distribution of immune cell subpopulations across the PBS, AI-sEV, and PD-L1 treatment groups. T-SNE plot of T-cell subpopulations, color-coded by (F) cell clusters, (G) cell types, and (H) sample groups. (I) Bar plot depicting the ratio of T cell subpopulations across treatment groups. (J) T-SNE plots visualizing the gene expression patterns of *Gzma*, *Gzmb*, *Ifng*, and *Tnf* across T cells, illustrating the spatial distribution of these genes within T cell clusters. (K) KEGG enrichment analysis for proliferating T cells. The analysis focuses on genes upregulated in the AI-sEV treatment group, highlighting key activated pathways associated with these T cell states. (L) The developmental trajectory of T cell types inferred by Monocle2. (M) Pseudotime analysis with dark blue indicating the starting point, the arrow denoting the trajectory across pseudotime, and light blue representing the end of pseudotime.

differentiation, and T cell receptor signaling pathway) in proliferating T cells following AI-sEV treatment (Fig. 6K). Similarly, GO enrichment analysis confirmed enrichment of pathways related to T cell activation and proliferation (Supporting Information Fig. S42). Pseudotime trajectory analysis using Monocle2 further supported the observed effects of AI-sEVs on T cell differentiation and activation. Naïve and immature T cells were predominantly located at the early stage of the trajectory, while effector T cells, proliferating T cells, exhausted T cells, and cytotoxic T cells occupied the terminal phase (Fig. 6L and M). Grouped pseudotime analysis demonstrated a significant reduction in naïve and immature T cells at the initiation stage in AI-sEV-treated samples, suggesting their differentiation into effector and cytotoxic T cell populations (Supporting Information Fig. S43A−S43C). Additionally, gene expression trends observed throughout this differentiation process further supported the notion of T cell activation followed by eventual exhaustion during the immune response (Fig. S43D).

In summary, integrative analyses, including t-SNE clustering, enrichment studies, and pseudotime trajectory mapping, demonstrated that AI-sEVs not only activate cytotoxic T cells but also drive effector T cell differentiation. These effects underscore the pivotal role of AI-sEVs in enhancing anti-tumor immunity within the NSCLC microenvironment.

3.6. AI-sEVs modulate NK cells and B cells to activate immune stimulation

Beyond their effects on T cells, AI-sEVs also modulated the phenotypic and functional states of NK and NKT cells in NSCLC. ScRNA-seq analysis revealed distinct clustering patterns among PBS-, PD-L1-, and AI-sEV-treated groups (Fig. 7A and B). Based on their differentiation stages, NK and NKT cells were further subdivided into 10 distinct subclusters to capture their phenotypic heterogeneity (Fig. 7C). Notably, NKT_5 cells, which resembled tissue-resident-like NKT cells with reduced activity, were predominantly enriched in the PBS group and largely absent in the AI-sEV group (Fig. 7D). In contrast, AI-sEV treatment significantly elevated the abundance of several other clusters—specifically NK_1, NK_2, NK_6, NK_7, and NK_8—most of which were composed of activated NK cell subsets. These AI-sEV-expanded NK subpopulations exhibited elevated expression of genes encoding effector molecules (*Ifng*, *Tnf*, *Prf1*, and *Gzma)* and transcription factors linked to NK cell activation (*Cxcl10*, *Ccl3*, *Ccl4*, and *Il12rb2*) (Supporting Information Fig. S44). NK_8 cells particularly expressed high levels of proliferation-associated markers (*Irf8*, *Pclaf*, *Dut*, and *Stmn1*), indicative of enhanced proliferation and immune infiltration (Fig. 7E). GO enrichment analyses further revealed that AI-sEV-expanded NK and NKT cells engaged in antigen recognition and rapid immune responses, leading to upregulation of immune-related pathways, particularly response to interferon-gamma and positive regulation of lymphocyte activation pathways (Supporting Information Fig. S45). The trajectory branched into two distinct lineages, with conventional NK cells occupying the early segment and differentiated NKT cells enriched at the terminal ends (Fig. 7F and G, Supporting Information Fig. S46). These findings underscore the roles of NK and NKT subsets in shaping the TME by secreting effector molecules and upregulating activation-related transcription factors. AI-sEV-activated NK cells particularly functioned as key mediators linking innate and adaptive immunity, enhancing the maturation and functional engagement of other immune populations within the TME.

Tumor-infiltrating B cells (TIBs) also demonstrated significant heterogeneity following treatment. We identified eight distinct B cell clusters, including five key functional subtypes: naïve B cells, memory B cells, inflammatory plasma cells, germinal center B (GCB) cells, and activated B cells (Fig. 7H and I). Comparative analysis revealed that the memory B cell and GCB clusters were significantly expanded by AI-sEV treatment (Fig. 7I and J, Supporting Information Fig. S47). B_4 and B_5 were identified as GCB-like subpopulations, characterized by their role in generating high-affinity antibodies and facilitating memory B cell differentiation. Additionally, B_1 and B_3 exhibited memory B cell phenotypes, albeit with subtle differences in gene expression profiles (Fig. 7K). Specifically, B_1 (*Ccr7*, *Cxcr4*, *Plk2*, and *Klf4*) displayed canonical memory B cell features, whereas B_3 was distinguished by low *Ccr7* expression, suggesting an atypical memory B cell subtype (Fig. 7L). Notably, naïve B cells were significantly increased following AI-sEV treatment, which may be attributed to the IL-7 encapsulated within AI-sEVs. This cytokine promotes B cell development and progenitor B cell proliferation in the bone marrow, thereby enhancing the output of naïve B cells. Trajectory inference analysis further elucidated the differentiation pathway from naïve B cells through GCB intermediates, leading to multiple differentiation branches—one primarily representing activated B cells, and the other culminating in memory B cell formation (Fig. 7M and N, Supporting Information Fig. S48). Collectively, AI-sEVs orchestrated a broad reprogramming of the NSCLC TME, promoting NK/NKT cell activation and B cell maturation. These immunomodulatory effects potentiated both innate and adaptive immune responses, potentially accounting for the superior therapeutic efficacy associated with AI-sEV treatment.

3.7. Antitumor evaluation of AI-sEVs in a humanized PDX (hu-PDX) model

To further evaluate the therapeutic efficacy of AI-sEVs within a patient-relevant TME, we established a hu-PDX model by intravenously injecting human peripheral blood mononuclear cells (PBMCs), thereby recapitulating key aspects of clinical immunotherapy settings (Fig. 8A). Once tumor volumes reached $\sim$200 mm^3, immunohistochemistry was performed on primary LUAD tissues, as well as serially passaged G1−G3 xenografts, confirming stable expression of human leukocyte antigen (HLA), and validating successful tumor engraftment and maintenance of human tumor characteristics (Fig. 8B). The humanization efficiency of the murine immune system was tracked by quantifying human $CD45^+$ cells among total lymphocytes at weekly intervals (weeks 1−4) post-PBMC infusion. Human $CD45^+$ cell frequencies progressively increased, reaching 53% by Week 4 (Fig. 8C). Upon confirmation of immune reconstitution, mice were randomized into three treatment groups: PBS control, anti-PD-L1 antibody, and AI-sEVs. No significant differences in body weight or food intake were observed, indicating good treatment tolerability (Supporting Information Fig. S49A). AI-sEV treatment resulted in a robust tumor suppression, with a 78% reduction in tumor volume, outperforming anti-PD-L1 therapy, which achieved $\sim$42% inhibition (Fig. 8D and E, Fig. S49B). Histological analysis of PBS-treated tumors revealed densely packed tumor cells with minimal immune infiltration. In contrast, AI-sEV-treated tumors displayed sparse cellularity and extensive necrosis, as shown by H&E staining (Fig. 8F). Ki67 staining further demonstrated a significant reduction in tumor proliferation following AI-sEV treatment (Fig. 8F).

To investigate whether AI-sEVs exert similar effects on autophagy inhibition and MHC-I expression in the hu-PDX model as observed in orthotopic models, we examined IL-7, autophagy markers, and MHC-I expression. IL-7 was negligible in untreated PDX tumors but was significantly upregulated following AI-sEV treatment, confirming successful tumor-targeted delivery (Fig. 8F and G). Immunoblotting and IF confirmed suppressed autophagic activity, as evidenced by decreased levels of LC3II/I, Beclin-1, ATG7, and p62 (Fig. 8G and H). Moreover, AI-sEVs enhanced MHC-I expression while reducing its co-localization with lysosomes (Fig. 8I), indicating effective inhibition of autophagic degradation and preservation of MHC-I antigen presentation machinery.

We next assessed whether AI-sEVs could enhance anti-PD-L1 immunotherapy by evaluating T cell responses. Flow cytometry analysis demonstrated a significant increase in $CD8^+$ T cells

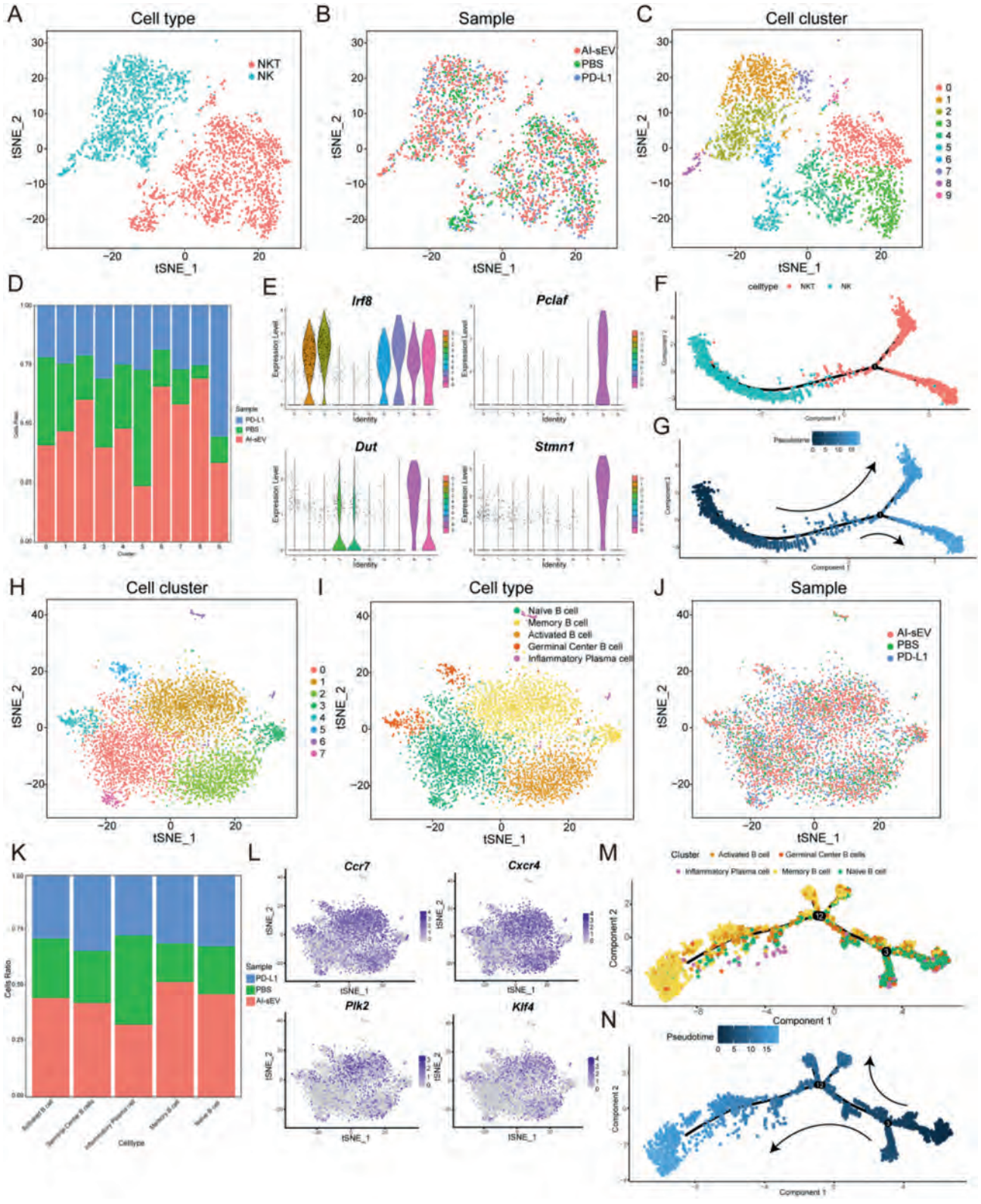

Figure 7 AI-sEVs modulate NK cells and B cells to activate immune stimulation. T-SNE plots of NK and NKT cell subpopulations, color-coded by (A) cell types, (B) treatment groups, and (C) cell clusters. (D) Bar plot depicting the proportion of NK and NKT cell subpopulations across different treatment conditions. (E) Violin plot illustrating the expression levels of *Irf8*, *Pclaf*, *Dut*, and *Stmn1* in NK and NKT cell clusters. (F) Pseudotime trajectory analysis of NK and NKT cell subclusters with clustering by cell type. (G) Pseudotime analysis with dark blue indicating the starting point, the arrow denoting the trajectory across pseudotime, and light blue representing the end of pseudotime. T-SNE plot of B cell subpopulations, color-coded by (H) cell cluster, (I) cell types, and (J) treatment group. (K) Bar plot depicting the proportion of B cell subpopulations across treatment conditions. (L) T-SNE projections of gene expression patterns for *Ccr7*, *Cxcr4*, *Plk2*, and *Klf4*. Pseudotime trajectory analysis of B cell subclusters grouped by (M) cell types. (N) Pseudotime analysis with dark blue indicating the starting point, the arrow denoting the trajectory across pseudotime, and light blue representing the end of pseudotime.

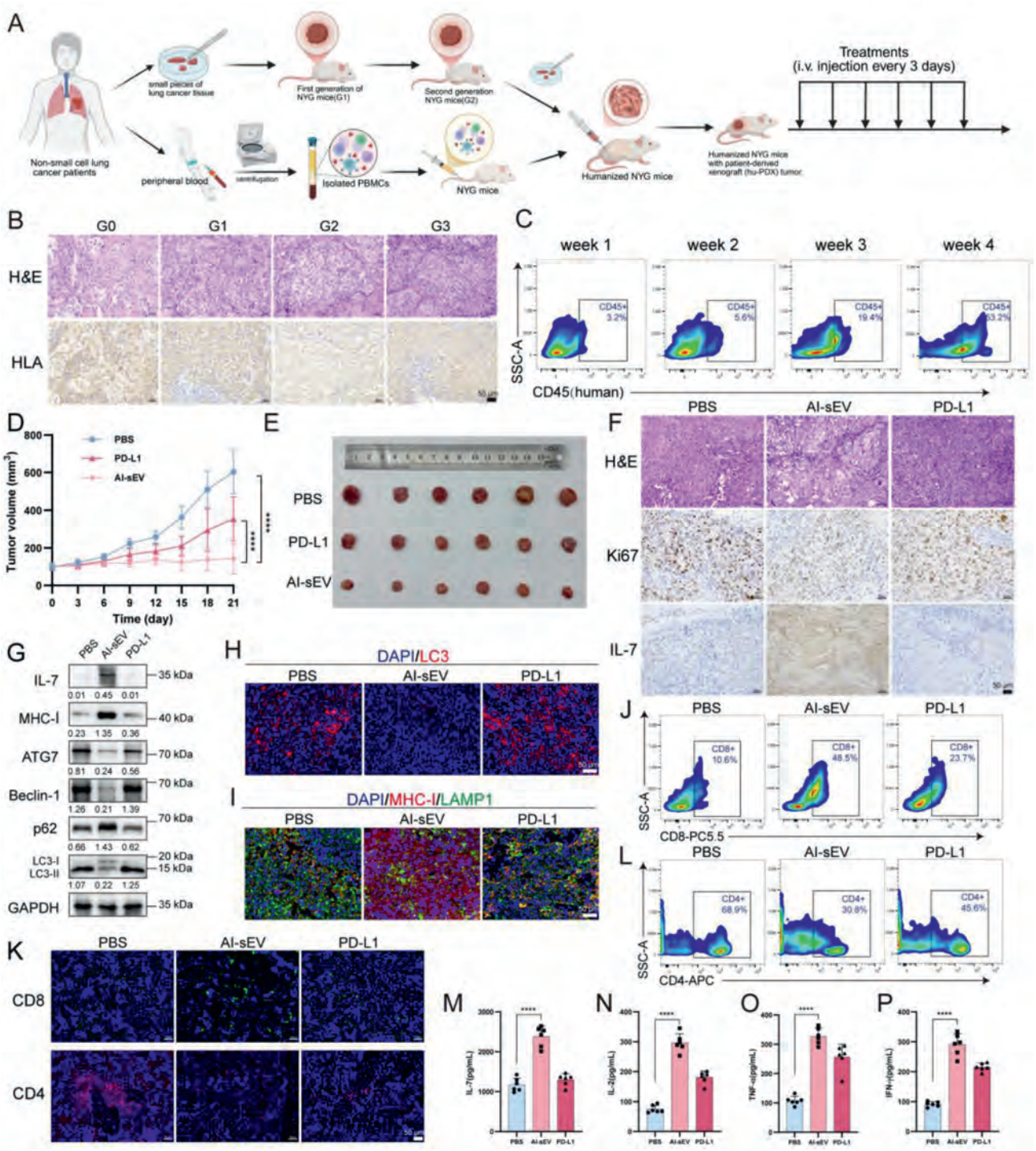

Figure 8 Antitumor evaluation of AI-sEVs in a hu-PDX model. (A) Schematic representation of AI-sEVs administration in the hu-PDX model. (B) Histopathologic structures of lung cancer tissues from patients with LUAD in different generations of the PDX mouse model, as demonstrated by H&E staining and IHC. Scale bar: 50 μm. (C) Flow cytometric analysis of humanized $CD45^+$ cells among mouse lymphocytes at Weeks 1−4 post-reinfusion of humanized PBMCs. (D) Tumor volume curves following treatment with PBS, anti-PD-L1, and AI-sEV ($n = 6$). (E) Representative images of tumors after treatment with PBS, anti-PD-L1, and AI-sEVs ($n = 6$). (F) Histopathological analysis of tumor tissues using H&E staining and proliferation marker Ki67 and IL-7 expression by IHC. Scale bar: 50 μm. (G) Western blot analysis of IL-7, MHC-I, autophagy-associated proteins (ATG7, Beclin-1, p62, and LC3) in tumor tissues. (H) IF staining of LC3 in tumor tissues. Scale bar: 50 μm. (I) Co-IF staining of MHC-I and LAMP1 in tumor tissues. Scale bar: 50 μm. Flow cytometric analysis of (J) $CD8^+$ T and (L) $CD4^+$ T cells in tumor tissues from the hu-PDX model. (K) Tissue IF analysis of CD8 and CD4 in spleen tissues. Scale bar: 50 μm. Quantification of (M) IL-7 and effector cytokines ((N) IL-2, (O) TNF-α, (P) IFN-γ) in tumor homogenate supernatants using ELISA ($n = 6$). Data in (D), (M−P) are illustrated as mean ± SD. Statistical significance was calculated by Student's *t*-test and one-way ANOVA with Tukey's multiple comparisons test. $^*P < 0.05$, $^{**}P < 0.01$, $^{***}P < 0.001$, $^{****}P < 0.0001$.

within tumor and spleen tissues, indicating enhanced activation and an augmented anti-tumor immune response (Fig. 8J and K). Concurrently, a decrease in $CD4^+$ T cell counts and elevated levels of T cell effector cytokines (IL-2, TNF-α, IFN-γ) further substantiated the immunostimulatory effect of AI-sEVs (Fig. 8K−P). Meanwhile, no significant organ damage or abnormalities in serum AST, ALT, Cr, and BUN levels were observed (Supporting Information Fig. S50), suggesting a favorable safety profile. In summary, AI-sEVs demonstrated potent anti-tumor efficacy in a clinically relevant hu-PDX model by enhancing immune cell infiltration, suppressing tumor proliferation, inhibiting autophagy, and preserving MHC-I expression. Their ability to synergize with PD-L1 blockade while maintaining systemic safety supports their promise as a next-generation immunotherapeutic platform for NSCLC.

4. Discussion

In this study, we developed tumor-targeted multifunctional AI-sEVs that effectively overcame two critical barriers to antitumor immunity in NSCLC: defective antigen presentation and PD-1/PD-L1-mediated immunosuppression. By integrating receptor-specific targeting peptides, AI-sEVs achieve selective delivery to NSCLC cells, leveraging overexpressed surface markers for precise tumor localization. Building upon established evidence that tumors evade $CD8^+$ T cell surveillance through MHC-I downregulation *via* lysosomal proteolysis and NBR1-mediated selective autophagy[19,44,45], we designed AI-sEVs to incorporate *IL*-7 mRNA, thereby modulating autophagy through IL-7 signaling. This strategy preserves MHC-I surface expression by blocking lysosomal degradation, restoring tumor immunogenicity. The platform exerts synergistic effects through three interlinked mechanisms. First, IL-7-mediated autophagy inhibition stabilizes MHC-I complexes on tumor cells, reversing the lysosomal degradation pathway typically exploited for immune evasion. Second, enhanced MHC-I presentation, which increases the visibility of tumor neoantigens to $CD8^+$ T cells, revitalizes their cytotoxic recognition capacity. Third, PD-1/PD-L1 immune checkpoint blockade, which amplifies T cell activation and sustains anti-tumor immune responses. Mechanistically, our results reveal that autophagy suppression is a critical prerequisite for effective MHC-I restoration. Notably, excessive lysosomal activity significantly limits the efficacy of PD-1/PD-L1 blockade alone, underscoring the need for combinatorial intervention. In both orthotopic and hu-PDX models, AI-sEV treatment significantly outperformed monotherapies, as evidenced by greater tumor control, enhanced $CD8^+$ T cell infiltration, and upregulation of T cell activation signatures. These findings establish the therapeutic advantage of coordinated targeting of antigen presentation machinery and immune checkpoint pathways. This strategy effectively converts immunologically "cold" NSCLC tumors into T cell-inflamed microenvironment, while simultaneously enhancing anti-tumor activity.

Analysis of the TCGA database and clinical cases revealed a significant reduction in IL-7 expression in LUAD and LUSC, which was associated with poor prognosis. IL-7 plays a crucial role in the TME and immunotherapy by promoting T cell differentiation and maintaining effector T cells[46]. Furthermore, IL-7 has been shown to sustain $CD8^+$ T cell responses by inhibiting PD-1 expression on T cells[47], as well as enhancing immune cell infiltration within tumors[48]. Our research establishes a novel association between IL-7 signaling and autophagy regulation in NSCLC. Although autophagy has a dual role in tumorigenesis and progression, it remains a compelling therapeutic target due to its pro-survival function in tumor cells under stress[49]. On one hand, NBR1-mediated selective autophagy accelerates the lysosomal degradation of MHC-I, which directly impairs $CD8^+$ T cell antigen recognition and contributes to immune escape. On the other hand, autophagy positively supports T cell activation and memory formation[50]. Given that AI-sEVs primarily deliver their cargo to tumor cells, and accumulating evidence supports autophagy inhibition as a strategy to enhance immunotherapy efficacy, we adopted a strategy combining autophagy inhibition with immunotherapy[51]. For example, concurrent targeting of CD47 and autophagy has been shown to increase macrophage phagocytosis of lung cancer cells[52]. The limited efficacy of PD-1/PD-L1 monotherapy in tumors with low MHC-I expression, combined with the poor prognosis of NSCLC patients who have low IL-7 expression, further supports this approach. These characteristics are consistent with an autophagy-driven immunosuppressive phenotype. In our strategy, *IL*-7 mRNA delivered by AI-sEVs activates the PI3K/AKT/mTOR signaling pathway, leading to the suppression of the key autophagy regulator Beclin-1, thereby inhibiting autophagy. This approach, when combined with PD-L1 blockade, simultaneously overcomes two significant barriers: defective antigen presentation and immune checkpoint inhibition, resulting in significantly superior therapeutic outcomes compared to monotherapy. Nevertheless, it is crucial to emphasize that autophagy-targeting strategies should be combined with immune modulators and applied within a spatiotemporally defined "therapeutic window" to block tumor immune evasion while promoting effective antitumor immunity. In the current study, using an immunotherapy tumor model characterized by high intrinsic autophagic flux, the combination of autophagy inhibition with immune checkpoint blockade achieves maximal therapeutic benefit. Furthermore, selectively inhibiting Beclin-1 through IL-7-activated PI3K/AKT/mTOR signaling may reduce potential toxicity to normal cells, as this approach avoids widespread suppression of autophagy. Additionally, the tumor-targeting delivery capability of AI-sEVs enhances the precision of this intervention, minimizing off-target effects and improving therapeutic safety.

To achieve precise delivery of *IL*-7 mRNA to the tumor-infiltrating region, we developed a scalable method. By combining nanosecond pulsed electroporation with ultrasound stimulation, we significantly increased both sEV yield and transfection efficiency, while maintaining cell viability. This approach was further refined using a microinjection pump-driven system for high-throughput production, incorporating automated cell seeding and ultrasonic nozzle-based dispersal. HEK293T cells were selected as the source for EV production to achieve higher yields and improved transfection efficiency of sEVs. HEK293T-derived sEVs contain minimal endogenous cargo and lack molecular inducers of disease-related pathways, thereby minimizing the potential transfer of unintended or undesirable components[53]. Moreover, the inherently low expression levels of MHC I/II molecules in these sEVs confer a naturally low immunogenic profile[54]. To enhance nucleic acid loading and release, we tethered *IL*-7 mRNA to the transmembrane protein CD64 *via* the Rev ARM peptide, which selectively binds the RRE-IIB RNA motif[55,56]. The RRE-IIB/Rev ARM system achieves highly specific recognition through a dual mechanism involving structural complementarity and electrostatic-mediated specificity. A cathepsin B−cleavable polypeptide linker, $(GFLG)_3$, was inserted between CD64 and Rev ARM peptide to facilitate mRNA release in the acidic, cathepsin B-rich TME[57]. In addition, the extracellular domain of

CD64 served as an Fcγ type I receptor, enabling the conjugation of anti-PD-L1 antibodies. This dual-targeting configuration enables modular antibody loading, allowing for the potential co-delivery of multiple checkpoint inhibitors when optimally balanced.

Functionally, AI-sEVs co-delivery of *IL*-7 mRNA and anti-PD-L1 antibody successfully reprogrammed the TME. It converted immunologically "cold" tumors into "hot" ones by increasing MHC-I expression, restoring immune surveillance, and inhibiting tumor progression. ScRNA-seq results reveal that AI-sEVs achieve multi-level remodeling of the immunosuppressive TME in NSCLC by driving lymphocyte activation and functional differentiation. Detailed subclustering analyses of T, B, and NK cells provided insights into the distinct roles of various lymphocyte subtypes within the AI-sEV-modulated NSCLC TME. AI-sEVs promote the early differentiation of naïve T cells into cytotoxic and effector phenotypes, significantly expanding effector T cell ($TNF^+IFN\text{-}\gamma^+$) and cytotoxic T cell ($GZMA/B^+$) subsets while reducing the proportion of naïve/immature T cells. Additionally, they reprogram exhausted T cells into an immunologically active state, characterized by co-expression of effector molecules (CCL3/4) and co-stimulatory receptors (TNFRSF9/4). Beyond their effects on T cells, AI-sEVs also activate NK/NKT cell immunity, expanding proliferative ($IRF8^+STMN1^+$) and effector ($PRF1^+IFNG^+$) subsets while suppressing tissue-resident quiescent NKT cells, thereby further stimulating immune infiltration. Notably, the mechanisms underlying the enhanced NK cell activity induced by AI-sEV treatment remain to be fully elucidated and require further investigation. Moreover, AI-sEVs facilitate B-cell maturation through germinal center and memory B-cell differentiation. The synergistic reprogramming induced by AI-sEVs enhances innate-adaptive immune interactions, thereby amplifying the effects of tumor cell killing. Integrative single-cell profiling demonstrates that AI-sEVs reshape the NSCLC immune landscape *via* coordinated lymphocyte reprogramming: catalyzing T cell effector differentiation, activating exhausted T cell subsets, expanding cytotoxic NK populations, and promoting B cell memory maturation. This multi-tiered reconstruction of innate and adaptive immunity forms the molecular basis for the superior antitumor efficacy of AI-sEVs. These findings collectively underscore the potential of AI-sEVs as a novel therapeutic strategy for enhancing anti-tumor immunity in NSCLC. Compared to systemic administration *via* tail vein injection, inhalational delivery of sEVs demonstrates superior therapeutic efficacy in lung cancer treatment, highlighting the potential of localized delivery for respiratory tract malignancies[58]. However, the generalizability of this route to other tumor types remains to be evaluated.

In conclusion, AI-sEVs represent a tumor-targeted, safe, and long-circulating drug delivery system capable of reversing autophagy-mediated immune suppression within the TME. Its dual-function design not only enhances antigen presentation and immune activation but also provides a versatile platform for combination immunotherapy. Future studies should focus on optimizing this delivery system for broader clinical applicability across diverse solid tumors and refining the mechanisms by which AI-sEVs modulate innate and adaptive immune responses.

5. Conclusions

In summary, this study establishes AI-sEV as a tumor-targeted, synergistic therapeutic platform that overcomes key immune evasion mechanisms in NSCLC, including autophagy-mediated MHC-I degradation and PD-1/PD-L1 immunosuppression. By delivering *IL*-7 mRNA to inhibit autophagy and restore MHC-I presentation while concurrently blocking PD-1/PD-L1, AI-sEVs transform immunologically "cold" NSCLC tumors into T cell-inflamed microenvironments. This coordinated strategy significantly outperforms monotherapies, enhancing tumor control and $CD8^+$ T cell activity in preclinical models, highlighting the suppression of autophagy as a critical prerequisite for effective immunotherapy.

Acknowledgments

This study was supported by the National Natural Science of China (82572406, Zhaogang Yang; 82372696, Xiaobing Wang), Foundation of Jilin Science-Technology Committee (20250206003 ZP, Zhaogang Yang, China), Graduate Innovation Fund of Jilin University (2025CX129, Jiayi Chen, China), and Jilin University Doctoral Student Research and Innovation Enhancement Program (2025KC038, Yaxin Cui, China).

Author contributions

Zhaogang Yang, Simiao Wang, and Xiaobing Wang conceptualized the study, and Zhaogang Yang supervised experiments. Simiao Wang and Jiayi Chen designed and performed the study. Yaxin Cui, Jianming Xing, and Hongqun Yang analyzed the scRNA-seq and RNA-seq data. Simiao Wang, Jiayi Liu, and Hao Jiang wrote the paper. Huan Zhang performed the biochemical experiments. Simiao Wang and Man Sun performed the cellular and animal experiments. Jialin Li and Wei Liu helped with animal experiments. Zhou Chen, Wei Sun, Xiaobing Wang, and Zhaogang Yang provided critical comments and suggestions. All authors read and contributed to the final manuscript.

Conflicts of interest

The authors declare no conflicts of interest.

Appendix A. Supporting information

Supporting information to this article can be found online at https://doi.org/10.1016/j.apsb.2025.12.013.

References

1. Sung H, Ferlay J, Siegel RL, Laversanne M, Soerjomataram I, Jemal A, et al. Global cancer statistics 2020: GLOBOCAN estimates of incidence and mortality worldwide for 36 cancers in 185 countries. *CA Cancer J Clin* 2021;**71**:209−49.
2. Oser MG, Niederst MJ, Sequist LV, Engelman JA. Transformation from non-small-cell lung cancer to small-cell lung cancer: molecular drivers and cells of origin. *Lancet Oncol* 2015;**16**:e165−72.
3. Rosell R, Karachaliou N. Large-scale screening for somatic mutations in lung cancer. *Lancet* 2016;**387**:1354−6.
4. Sasaki T, Seto T, Yamanaka T, Kunitake N, Shimizu J, Kodaira T, et al. A randomised phase II trial of S-1 plus cisplatin *versus* vinorelbine plus cisplatin with concurrent thoracic radiotherapy for unresectable, locally advanced non-small cell lung cancer: WJOG5008L. *Br J Cancer* 2018;**119**:675−82.
5. Zhong WZ, Yan HH, Chen KN, Chen C, Gu CD, Wang J, et al. Erlotinib *versus* gemcitabine plus cisplatin as neoadjuvant treatment

of stage IIIA-N2 EGFR-mutant non-small-cell lung cancer: final overall survival analysis of the EMERGING-CTONG 1103 randomised phase II trial. *Signal Transduct Targeted Ther* 2023;**8**:76.
6. Vokes EE, Ready N, Felip E, Horn L, Burgio MA, Antonia SJ, et al. Nivolumab *versus* docetaxel in previously treated advanced non-small-cell lung cancer (CheckMate 017 and CheckMate 057): 3-year update and outcomes in patients with liver metastases. *Ann Oncol* 2018;**29**:959−65.
7. Herbst RS, Baas P, Kim DW, Felip E, Pérez-Gracia JL, Han JY, et al. Pembrolizumab *versus* docetaxel for previously treated, PD-L1-positive, advanced non-small-cell lung cancer (KEYNOTE-010): a randomised controlled trial. *Lancet* 2016;**387**:1540−50.
8. Rittmeyer A, Barlesi F, Waterkamp D, Park K, Ciardiello F, von Pawel J, et al. Atezolizumab *versus* docetaxel in patients with previously treated non-small-cell lung cancer (OAK): a phase 3, open-label, multicentre randomised controlled trial. *Lancet* 2017;**389**:255−65.
9. Antonia SJ, Villegas A, Daniel D, Vicente D, Murakami S, Hui R, et al. Overall survival with durvalumab after chemoradiotherapy in stage III NSCLC. *N Engl J Med* 2018;**379**:2342−50.
10. Sharma P, Hu-Lieskovan S, Wargo JA, Ribas A. Primary, adaptive, and acquired resistance to cancer immunotherapy. *Cell* 2017;**168**:707−23.
11. Huang C, Wang X, Wang Y, Feng Y, Wang X, Chen S, et al. Sirpα on tumor-associated myeloid cells restrains antitumor immunity in colorectal cancer independent of its interaction with CD47. *Nat Cancer* 2024;**5**:500−16.
12. Horvath L, Thienpont B, Zhao L, Wolf D, Pircher A. Overcoming immunotherapy resistance in non-small cell lung cancer (NSCLC)—Novel approaches and future outlook. *Mol Cancer* 2020;**19**:141.
13. Wang H, Franco F, Tsui YC, Xie X, Trefny MP, Zappasodi R, et al. CD36-mediated metabolic adaptation supports regulatory T cell survival and function in tumors. *Nat Immunol* 2020;**21**:298−308.
14. Duan Y, Hu Z, Han P, Lei B, Wang S, Wang Z, et al. ADSL-generated fumarate binds and inhibits STING to promote tumour immune evasion. *Nat Cell Biol* 2025;**27**:668−82.
15. Boreel DF, Span PN, Heskamp S, Adema GJ, Bussink J. Targeting oxidative phosphorylation to increase the efficacy of radio- and immune-combination therapy. *Clin Cancer Res* 2021;**27**:2970−8.
16. Liu Z, Wang T, She Y, Wu K, Gu S, Li L, et al. N^6-Methyladenosine-modified circIGF2BP3 inhibits $CD8^+$ T-cell responses to facilitate tumor immune evasion by promoting the deubiquitination of PD-L1 in non-small cell lung cancer. *Mol Cancer* 2021;**20**:105.
17. Sinclair LV, Youdale T, Spinelli L, Gakovic M, Langlands AJ, Pathak S, et al. Autophagy repression by antigen and cytokines shapes mitochondrial, migration, and effector machinery in CD8 T cells. *Nat Immunol* 2025;**26**:429−43.
18. Jiang GM, Tan Y, Wang H, Peng L, Chen HT, Meng XJ, et al. The relationship between autophagy and the immune system and its applications for tumor immunotherapy. *Mol Cancer* 2019;**18**:17.
19. Yamamoto K, Venida A, Yano J, Biancur DE, Kakiuchi M, Gupta S, et al. Autophagy promotes immune evasion of pancreatic cancer by degrading MHC-I. *Nature* 2020;**581**:100−5.
20. Bozic M, Wilkinson S. Selective autophagy conceals the enemy: why cytotoxic T cells don't (MH)C pancreatic cancer. *Mol Cell* 2020;**79**:6−8.
21. Xue Y, Yan X, Li D, Dong S, Ping Y. Proinflammatory polarization of engineered heat-inducible macrophages reprogram the tumor immune microenvironment during cancer immunotherapy. *Nat Commun* 2024;**15**:2270.
22. Zhang R, Yu C, Zeh HJ, Kroemer G, Klionsky DJ, Tang D, et al. TAX1BP1-dependent autophagic degradation of STING1 impairs antitumor immunity. *Autophagy* 2025;**21**:1802−23.
23. Zhu Y, Jiang X, Ding Z, Ming J. Interleukin 7 inhibit autophagy *via* P53 regulated AMPK/mTOR signaling pathway in non-small cell lung cancer. *Sci Rep* 2022;**12**:11208.
24. Cui G, Staron MM, Gray SM, Ho PC, Amezquita RA, Wu J, et al. IL-7-induced glycerol transport and TAG synthesis promotes memory $CD8^+$ T cell longevity. *Cell* 2015;**161**:750−61.
25. Bae J, Liu L, Moore C, Hsu E, Zhang A, Ren Z, et al. IL-2 delivery by engineered mesenchymal stem cells re-invigorates $CD8^+$ T cells to overcome immunotherapy resistance in cancer. *Nat Cell Biol* 2022;**24**:1754−65.
26. Park KY, Kim SJ, Oh E, Heo TH. Induction of vascular leak syndrome by tumor necrosis factor-alpha alone. *Biomed Pharmacother* 2015;**70**:213−6.
27. Nash AM, Aghlara-Fotovat S, Castillio B, Hernandez A, Pugazenthi A, Lee HS, et al. Activation of adaptive and innate immune cells *via* localized IL2 cytokine factories eradicates mesothelioma tumors. *Clin Cancer Res* 2022;**28**:5121−35.
28. Zhang B, Sun J, Wang Y, Ji D, Yuan Y, Li S, et al. Site-specific PEGylation of interleukin-2 enhances immunosuppression *via* the sustained activation of regulatory T cells. *Nat Biomed Eng* 2021;**5**:1288−305.
29. Anselmo AC, Gokarn Y, Mitragotri S. Non-invasive delivery strategies for biologics. *Nat Rev Drug Discov* 2019;**18**:19−40.
30. Zhang H, Wang S, Sun M, Cui Y, Xing J, Teng L, et al. Exosomes as smart drug delivery vehicles for cancer immunotherapy. *Front Immunol* 2022;**13**:1093607.
31. Kalluri R, LeBleu VS. The biology, function, and biomedical applications of exosomes. *Science* 2020;**367**:eaau6977.
32. Liu Y, Zhang Y, Li H, Hu TY. Recent advances in the bench-to-bedside translation of cancer nanomedicines. *Acta Pharm Sin B* 2025;**15**:97−122.
33. Chen Y, Wang L, Zheng M, Zhu C, Wang G, Xia Y, et al. Engineered extracellular vesicles for concurrent anti-PDL1 immunotherapy and chemotherapy. *Bioact Mater* 2022;**9**:251−65.
34. Xiao T, Xiao Y, Wang W, Tang YY, Xiao Z, Su M. Targeting EphA2 in cancer. *J Hematol Oncol* 2020;**13**:114.
35. Wang X, Kwak KJ, Yang Z, Zhang A, Zhang X, Sullivan R, et al. Extracellular mRNA detected by molecular beacons in tethered lipoplex nanoparticles for diagnosis of human hepatocellular carcinoma. *PLoS One* 2018;**13**:e0198552.
36. Lee LJ, Yang Z, Rahman M, Ma J, Kwak KJ, McElroy J, et al. Extracellular mRNA detected by tethered lipoplex nanoparticle biochip for lung adenocarcinoma detection. *Am J Respir Crit Care Med* 2016;**193**:1431−3.
37. Wang S, Jiang H, Liu J, Chen J, Hu S, Cui Y, et al. LPAR4-targeted dual-loaded liposome for synergistic lung cancer therapy. *Eur J Pharmaceut Sci* 2025;**212**:107176.
38. Sun L, Wan AH, Yan S, Liu R, Li J, Zhou Z, et al. A multidimensional platform of patient-derived tumors identifies drug susceptibilities for clinical lenvatinib resistance. *Acta Pharm Sin B* 2024;**14**:223−40.
39. Zhou Z, Li X, Yang G, Wang J, Li B, Huang Y, et al. Targeting β-catenin and PD-L1 simultaneously by a racemic supramolecular peptide for the potent immunotherapy of hepatocellular carcinoma. *Theranostics* 2023;**13**:3371−86.
40. Zhang H, Xing J, Sun M, Cui Y, Li Y, Hu S, et al. Engineered exosomes for targeted microRNA delivery to reverse liver fibrosis. *Biomaterials* 2026;**324**:123510.
41. Sun M, Zhang H, Ma Y, Wang S, Chen J, Cui Y, et al. *In Situ* programming of the tumor microenvironment to alleviate immunosuppression for pancreatic cancer immunotherapy. *Adv Sci (Weinh)* 2025;**12**:e04008.
42. Sun D, Wu R, Zheng J, Li P, Yu L. Polyubiquitin chain-induced p62 phase separation drives autophagic cargo segregation. *Cell Res* 2018;**28**:405−15.
43. Sang W, Zhou Y, Chen H, Yu C, Dai L, Liu Z, et al. Receptor-interacting protein Kinase 2 is an immunotherapy target in pancreatic cancer. *Cancer Discov* 2024;**14**:326−47.
44. McGranahan N, Rosenthal R, Hiley CT, Rowan AJ, Watkins TBK, Wilson GA, et al. Allele-specific HLA loss and immune escape in lung cancer evolution. *Cell* 2017;**171**:1259−71.e11.
45. Lin W, Chen L, Zhang H, Qiu X, Huang Q, Wan F, et al. Tumor-intrinsic YTHDF1 drives immune evasion and resistance to immune checkpoint inhibitors *via* promoting MHC-I degradation. *Nat Commun* 2023;**14**:265.
46. Barata JT, Durum SK, Seddon B. Flip the coin: IL-7 and IL-7R in health and disease. *Nat Immunol* 2019;**20**:1584−93.

47. Hou L, Jie Z, Liang Y, Desai M, Soong L, Sun J. Type 1 interferon-induced IL-7 maintains $CD8^+$ T-cell responses and homeostasis by suppressing PD-1 expression in viral hepatitis. *Cell Mol Immunol* 2015;**12**:213−21.
48. Adachi K, Kano Y, Nagai T, Okuyama N, Sakoda Y, Tamada K. IL-7 and CCL19 expression in CAR-T cells improves immune cell infiltration and CAR-T cell survival in the tumor. *Nat Biotechnol* 2018;**36**: 346−51.
49. Yang H, Ni HM, Ding WX. The double-edged sword of MTOR in autophagy deficiency induced-liver injury and tumorigenesis. *Autophagy* 2019;**15**:1671−3.
50. Levy JMM, Towers CG, Thorburn A. Targeting autophagy in cancer. *Nat Rev Cancer* 2017;**17**:528−42.
51. Liu Y, Wang Y, Zhang J, Peng Q, Wang X, Xiao X, et al. Nanotherapeutics targeting autophagy regulation for improved cancer therapy. *Acta Pharm Sin B* 2024;**14**:2447−74.
52. Zhou H, Wang W, Xu H, Liang Y, Ding J, Lv M, et al. Metabolic reprogramming mediated by tumor cell-intrinsic type I IFN signaling is required for CD47-SIRPα blockade efficacy. *Nat Commun* 2024;**15**:5759.
53. Zhu X, Badawi M, Pomeroy S, Sutaria DS, Xie Z, Baek A, et al. Comprehensive toxicity and immunogenicity studies reveal minimal effects in mice following sustained dosing of extracellular vesicles derived from HEK293T cells. *J Extracell Vesicles* 2017;**6**:1324730.
54. Cheng Q, Dai Z, Smbatyan G, Epstein AL, Lenz HJ, Zhang Y. Eliciting anti-cancer immunity by genetically engineered multifunctional exosomes. *Mol Ther* 2022;**30**:3066−77.
55. Battiste JL, Mao H, Rao NS, Tan R, Muhandiram DR, Kay LE, et al. Alpha helix-RNA major groove recognition in an HIV-1 rev peptide−RRE RNA complex. *Science* 1996;**273**:1547−51.
56. Schneeberger EM, Halper M, Palasser M, Heel SV, Vušurović J, Plangger R, et al. Native mass spectrometry reveals the initial binding events of HIV-1 rev to RRE stem II RNA. *Nat Commun* 2020;**11**:5750.
57. Tam LKB, Chu JCH, He L, Yang C, Han KC, Cheung PCK, et al. Enzyme-responsive double-locked photodynamic molecular beacon for targeted photodynamic anticancer therapy. *J Am Chem Soc* 2023;**145**:7361−75.
58. Liu M, Hu S, Yan N, Popowski KD, Cheng K. Inhalable extracellular vesicle delivery of *IL-12* mRNA to treat lung cancer and promote systemic immunity. *Nat Nanotechnol* 2024;**19**:565−75.